ORIGINAL ARTICLE

Transition boundary between regular and Mach reflections for a moving shock interacting with a wedge in inviscid and polytropic argon

J. J. Gottlieb[1] · M. K. Hryniewicki[1] · C. P. T. Groth[1]

Abstract

The transition boundary separating the regions of regular and Mach reflections for a planar shock moving in argon and interacting with an inclined wedge in a shock tube is investigated using flow-field simulations produced by high-resolution computational fluid dynamics (CFD). The transition boundary is determined numerically using a modern and reliable CFD algorithm to solve Euler's inviscid equations of unsteady motion in two spatial dimensions with argon treated as a polytropic gas. This numerically computed transition boundary for inviscid flow, without a combined thermal and viscous boundary layer on the wedge surface, is determined by post-processing many closely stationed flow-field simulations to accurately determine the transition-boundary point when the Mach stem of the Mach-reflection pattern just disappears, and this pattern then transcends into that of regular reflection. The new numerical transition boundary for argon is shown to agree well with von Neumann's closely spaced sonic and extreme-angle boundaries for weak incident shock Mach numbers from 1.0 to 1.55, but it deviates upward and above the closely spaced sonic and extreme-angle boundaries by almost 2° at larger shock Mach numbers from 1.55 to 4.0. This upward trend of the numerical transition boundary for this sequel case with monatomic gases like argon ($\gamma = 5/3$) and no boundary layer on the wedge surface (inviscid flow) is similar to the previous finding for the case of diatomic gases and air ($\gamma = 7/5$). An alternative method used to determine one point on the transition boundary between regular and Mach reflections, from a collection of Mach-reflection patterns with a constant-strength shock and different far-field wedge angles, by linear and higher-order polynomial extrapolations to zero for triple-point trajectories versus wedge angle, is compared to the present method of using near-field data that are close to and surround the new transition boundary. Such extrapolation methods are shown to yield a different transition-boundary estimate that corresponds to the mechanical-equilibrium boundary of von Neumann. Finally, the significance of the computed inviscid transition boundary between regular and Mach reflections for monatomic and diatomic gases is explained relative to the case of viscous flow with a combined thermal and viscous boundary layer on the wedge surface.

Keywords Shock-wave reflection · Mach reflection · Regular to Mach reflection transition boundary · Regular reflection persistence

1 Introduction

The interaction of a planar shock wave of constant speed and amplitude with an inclined wedge or ramp in a shock-tube channel filled with a gas produces four basic shock-wave reflection configurations or patterns. These four patterns called regular reflection (RR), single-Mach reflection (SMR), transitional-Mach reflection (TMR), and double-Mach reflection (DMR) are illustrated in Fig. 1 by numerically generated flow-field images from computational fluid dynamics (CFD) simulations of shock-wave interactions with a ramp in argon. The SMR, TMR, and DMR patterns each have a Mach-stem shock (S_m) extending from the confluence point of the incident shock (S_i) and reflected shock (S_r) to the wedge surface, and they each feature a straight or curved slip stream or shear layer emanating from the triple-shock coalescence point toward the wedge surface, whereas

✉ J. J. Gottlieb
gottlieb@utias.utoronto.ca

1   Institute for Aerospace Studies, University of Toronto, 4925
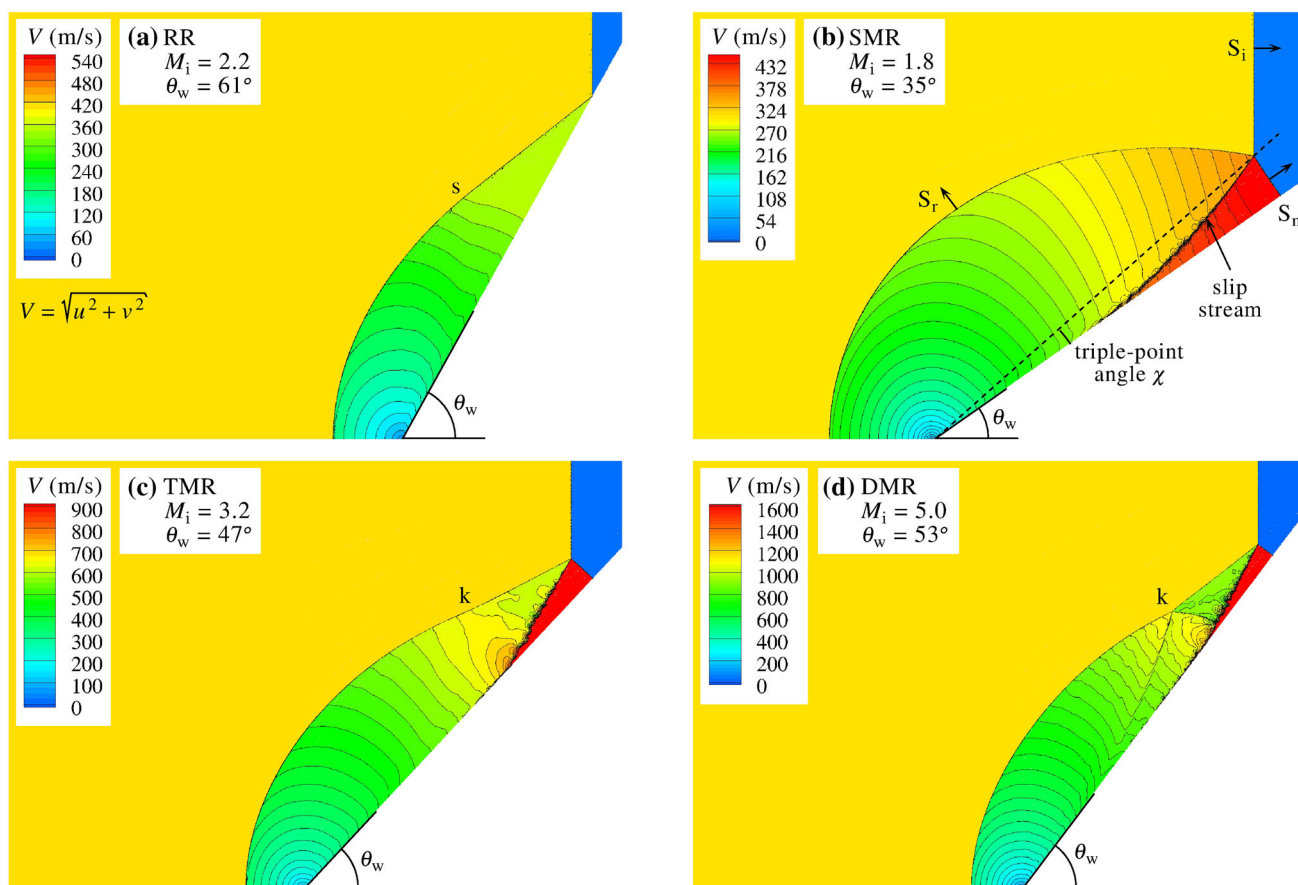   Dufferin Street, Toronto, ON M3H 5T6, Canada

Fig. 1 Flow-field images of regular- and Mach-reflection patterns from interactions of moving planar shock waves with an inclined wedge in argon. These images were computed numerically using the CFD algorithm mentioned in Sect. 2

the RR pattern has neither. The slope change and kink marked by s and k in the RR, TMR, and DMR configurations are the locations at which the initially straight reflected shock becomes curved thereafter, and a second slightly curved slip stream begins at location k only in the DMR pattern, whereas the reflected shock in the SMR pattern is completely curved. These s and k markers also denote the location at which the head of the so-called corner wave, disturbance, or signal contacts the reflected shock in the RR, TMR, and DMR patterns, whereas this corner wave has overtaken the Mach stem and triple point in the SMR configuration. In the case of TMR and DMR, the corner wave also contacts the subsonic flow field below the slip stream and has, therefore, also overtaken the Mach stem and triple point. However, the resulting disturbance from the altered flow behind the Mach stem is likely weak and has only slightly altered the flow on the upper side of the slip stream and possibly the straight portion and angle of the reflected shock.

The type of shock-reflection pattern that forms above the compression wedge depends on the strength of the incident shock (e.g., shock Mach number M_i), wedge angle (θ_w), and characteristics of the gas (e.g., without or with molecular vibration, dissociation, ionization, and chemical reactions). This dependence on shock strength and wedge angle is shown in Fig. 2 for the case of monatomic gases like argon, with the specific heat ratio $\gamma = 5/3$, by showing the transition boundaries between the regions of RR, SMR, TMR, and DMR. An important dual region of regular reflection (RR) and Mach reflection (MR) occurs when $M_i > 1.55$, in which the MR configurations are primarily TMR and DMR.

The three upper transition boundaries between regular and Mach reflections shown in Fig. 2 are based on three different criteria called mechanical equilibrium, extreme angle or detachment, and sonic flow. These analytical boundaries originate from von Neumann [1]. The sonic and extreme-angle boundaries are very close together, within half of a degree. The two other boundaries that subdivide the MR region into the regions of SMR, TMR, and DMR come from the research of Ben-Dor and Glass [2,3]. More information on Mach reflection is available in the books by Ben-Dor [4] and Glass and Sislian [5]. Ben-Dor [4] and Colella and Henderson [6] include another weak MR configuration named von Neumann reflection (vNR), which should occur in the left-hand side and bottom of the SMR region in Fig. 2, but

Fig. 2 Regions of RR and MR patterns separated by analytical transition boundaries for monatomic gases like argon ($\gamma = 5/3$), including experimental data for argon from experiments with a boundary layer on the wedge surface
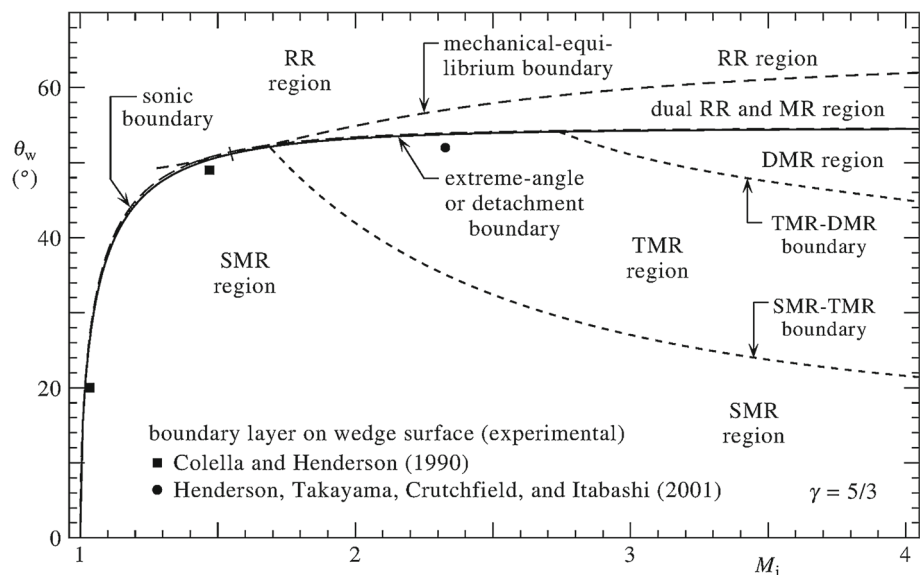
no boundary is available to map the vNR region therein. Ben-Dor[4] and Semenov et al.[7] provide more extensive classifications of Mach-reflection patterns, and Hornung[8] discusses RR-to-MR transition-boundary origins and criteria.

The three experimental data points shown in Fig. 2 stem from studies aimed specifically at finding transition-boundary points between RR and MR in argon, and in these shock-tube experiments a combined thermal and viscous boundary layer occurs on the wedge surface. Data were taken from a collection of shadowgraph, schlieren, or other photographs of Mach-reflection patterns on inclined wedges to plot the wedge angles (θ_w) versus triple-point angles (χ) (or some equivalent data), to help locate the transition-boundary point at which the angle χ (shown in Fig. 1b between the triple-point trajectory and wedge surface) diminishes to zero, at which the slip stream and Mach stem disappear.

The wedge angles θ_w for the first and second cases for a shock Mach number $M_i = 1.035$ and $M_i = 1.47$ in Fig. 2 were obtained by Colella and Henderson[6], by using an extrapolation of their data in their Figs. 4d and 3d, respectively. This was done for the case of a symmetric wedge with small effects from a wedge boundary layer, with a weighted extrapolation to the triple-point angle $\chi \rightarrow 0°$ to obtain the two wedge angles $\theta_w \approx 20°$ and $49°$. These extrapolations were considered reasonable in the opinion of the present authors because $M_i = 1.035$ and 1.47 are below the dual RR-to-MR region where flow property changes across the RR-to-MR transition boundary should be smooth, in contrast to rapid or discontinuous changes across the transition boundary in the dual RR and MR region mentioned by Bleakney and Taub[9] and Kawamura and Saito[10].

The wedge angle for the last case for $M_i = 2.237$ was obtained by the Henderson et al. [11]. This wedge angle stems

from special shock-tube experiments done with a wedge length of 0.17 m and for a wedge angle of $52°$. In one experiment, the wave pattern remains RR all along the wedge (their Fig. 13a), and in the second case the wave pattern starts as RR at the beginning of the wedge and switches over to MR just before the end of the wedge (their Fig. 13b). Hence, the transition from RR to MR is assumed herein by the authors to occur at $\theta_w = 52°$ for a wedge length of about 0.17 m. Other researchers have also planned and conducted shock-tube experiments to show that RR can change to MR along a wedge. For example, see Kobayashi et al.[12], who used a shock Mach number $M_i = 1.20$ and wedge angle $\theta_w \approx 40°$, so these data should define one point on the RR-to-MR transition boundary for a short 0.045-m-long wedge in air.

The experimental data from shock tubes presented in Fig. 2 for argon are sparse, partly because most researchers believed that the transition boundary between RR and MR for unsteady flows (with a moving incident shock wave) is located at or very close to von Neumann's closely spaced sonic and extreme-angle boundaries[4,8], so experiments might have been considered unnecessary for verification. However, one can imagine that a continuous experimental transition boundary exists between RR and MR, which passes through the three experimental data points shown in Fig. 2 and lies slightly below the extreme-angle boundary of von Neumann by $2°$–$3°$.

Similar experimental data for unsteady planar incident shock-wave reflections from ramps in diatomic gases and air, considered polytropic with $\gamma = 7/5$, are more numerous, as illustrated in Fig. 3. Such experimental results yield a more complete depiction of the transition boundary separating regular and Mach reflections. The black and black filled experimental markers for air that lie below the extreme-angle transition boundary [9,10,12–17], which were obtained in

Fig. 3 Regions of RR and MR patterns separated by analytical transition boundaries for diatomic gases and air ($\gamma = 7/5$), including experimental data for air with and without a boundary layer on the wedge surface
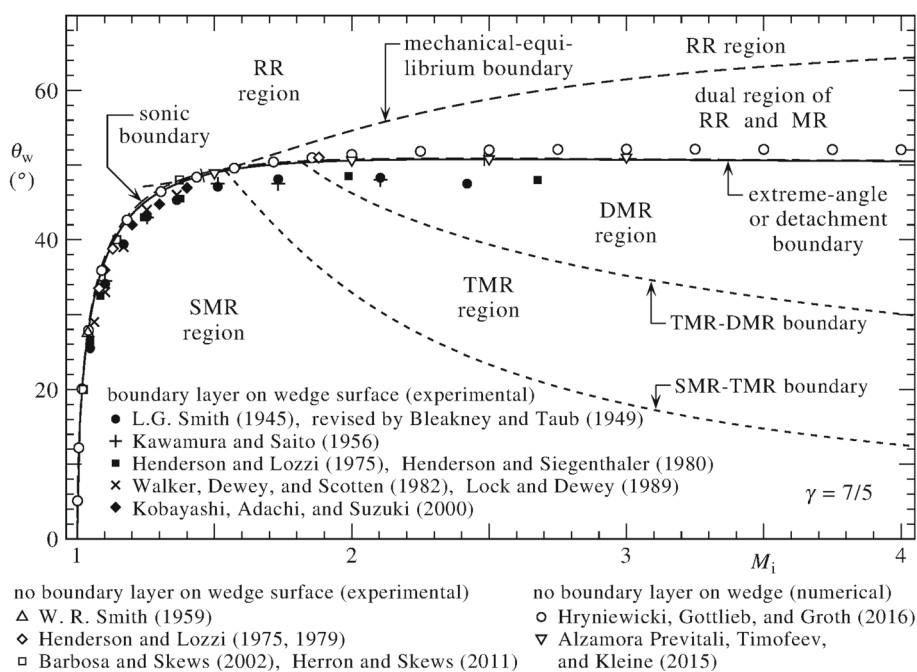
experiments with a combined thermal and viscous boundary layer on the wedge surface, show clearly that the experimental transition boundary between regular and Mach reflections lies a few degrees below the closely spaced sonic and extreme-angle boundaries.

The white filled experimental markers for diatomic gases and air [14,18–21] that lie near and on the closely spaced sonic and extreme-angle boundaries in Fig. 3 were obtained in special shock-tube experiments without a thermal and viscous boundary layer on the wedge surface, as explained in the papers by the respective authors and summarized in Sect. 5 of the paper by Hryniewicki et al. [22]. These experimental data illustrate that the closely spaced sonic and extreme-angle boundaries are reasonably good transition boundaries for incident shock Mach numbers M_i from 1.0 to 1.45, when the flow along the wedge surface is inviscid (i.e., without a boundary layer).

The set of numerically generated data for diatomic gases and air in Fig. 3, represented by the string of 20 white filled circles from Hryniewicki et al. [22], was generated by high-resolution numerical flow-field simulations and advanced post-processing techniques for the case of no thermal and viscous boundary layer on the wedge surface. This set of data for inviscid flow shows clearly that the transition boundary between RR and MR is in good agreement with the closely spaced sonic and extreme-angle boundaries of von Neumann for $1 < M_i < 1.45$. The white filled circles then trend above these two closely spaced boundaries by as much as several degrees for $M_i > 1.45$. This numerical transition boundary for air, represented by the string of data, is supported by all available experimental data for the case of no boundary

layer on the wedge surface. However, additional experimental data in the shock Mach number range of $2 < M_i < 4$ would be useful in confirming or disproving this newly discovered trend in the dual RR and MR region for inviscid shock reflections.

It should be noted that four numerically generated results for planar shock reflections from a straight wedge, without a boundary layer on the wedge in a diatomic gas, were computed by Alzamora Previtali et al. [23], and their results are included in Fig. 3. Although the plotted results for the three lower shock Mach numbers ($M_i = 1.5$, 2.0, and 2.5) agree fairly well with the closely spaced sonic and extreme-angle boundaries, the result for the higher Mach number ($M_i = 3.0$) lies definitely above the sonic boundary, by about 15–18% of the way from the sonic boundary to the new numerical transition boundary. This discovery of the existence of a Mach reflection occurring in the dual region above the sonic boundary was noted and discussed by Alzamora Previtali et al. [23], for the case of an inviscid flow of a diatomic gas. Furthermore, they also mentioned that a similar result for the case of argon is obtained in the paper by Henderson et al. [24].

All sets of experimental and numerical data shown in Fig. 3 for the case of diatomic gases and air illustrate the importance of including or excluding the combined thermal and viscous boundary layer on the wedge surface in terms of shifting the transition boundary between regular and Mach reflections. This shift is noticeable and significant and occurs from above to below the closely spaced sonic and extreme-angle boundaries of von Neumann, for the respective inviscid- and viscous-flow cases, with the largest

differences of about 4° for shock Mach numbers corresponding to those that define the dual RR and MR region.

One important objective of the present study is to extend the earlier numerical research by Hryniewicki et al. [22] for the case of diatomic gases and air (treated as a polytropic gas with $\gamma = 7/5$) to that for argon (treated similarly with $\gamma = 5/3$), to determine numerically the transition boundary separating regular and Mach reflections for argon with no boundary layer on the wedge surface. This is important in order to determine whether the upward shift of the inviscid transition boundary for diatomic gases and air occurs differently or similarly for the case of monatomic gases. Note that the effects of the specific heat ratio (γ) are moderate on the sonic, extreme-angle, mechanical-equilibrium, and other boundaries, but readily observable by comparing the results shown in Figs. 2 and 3. Most of the boundaries are shifted downward with a decrease in the value of γ and the dual RR and MR region becomes larger vertically because the mechanical-equilibrium boundary shifts upward for decreasing values of γ. The earlier investigation of diatomic gases and air [22] is prerequisite reading, because this study of monatomic gases is a sequel to the previous study.

The second objective of the present study is to illustrate that the method used in some previous investigations (e.g., [6,11,13,24]) of extrapolating a set of triple-point angles (χ) versus the wedge angle (θ_{w}) for MR patterns, for a given shock Mach number, to the location at which $\chi \rightarrow 0°$ can yield an incorrect RR-to-MR transition-boundary point, especially for incident shock Mach numbers corresponding to the dual RR and MR region. For the dual region, inappropriate extrapolations can lie near the mechanical-equilibrium boundary of von Neumann, and this sometimes results in the conjecture that the RR-to-MR transition boundary is the mechanical-equilibrium boundary.

The third and final objective of the present study is to clarify the significance of the single numerical transition boundary between RR and MR for the special case of inviscid flow when no boundary layer occurs on the wedge surface. The significance of this computed inviscid transition boundary is explained relative to the more relevant case of viscous flow with a boundary layer on the wedge surface, which is expected to feature multiple transition boundaries depending on the Reynolds number. This transition boundary for the viscous case is demonstrated to be wedge-surface length and roughness dependent.

2 Computational fluid dynamics solutions

The numerical solution of the partial differential equations governing two-dimensional unsteady compressible gas flows that are non-turbulent and inviscid is of interest herein for the determination of the unsteady flow fields for planar incident shock reflections from an inclined wedge without a combined thermal and viscous boundary layer. The partial differential equations of Euler for the conservation of mass, momentum, and energy [25] can be written in matrix form as

$$\frac{\partial \mathbf{U}}{\partial t} + \vec{\nabla} \cdot \vec{\mathbf{F}} = 0, \tag{1}$$

in which t denotes time and $\vec{\mathbf{F}} = (\mathbf{F}, \mathbf{G})$ is the total solution flux dyad. The three column vectors are

$$\mathbf{U} = \left[\rho, \ \rho u, \ \rho v, \ \rho e \right]^{\mathrm{T}}, \tag{2}$$

$$\mathbf{F} = \left[\rho u, \ \rho u^2 + p, \ \rho u v, \ u \left(\rho e + p \right) \right]^{\mathrm{T}}, \tag{3}$$

$$\mathbf{G} = \left[\rho v, \ \rho u v, \ \rho v^2 + p, \ v \left(\rho e + p \right) \right]^{\mathrm{T}}, \tag{4}$$

and they contain the conserved quantities (i.e., mass, x-momentum, y-momentum, total energy) and corresponding inviscid fluxes in the x- and y-coordinate directions. The superscript T denotes the matrix transpose. The symbols p, ρ, u, and v represent the gas pressure, density, and flow velocities in the x- and y-coordinate directions. The total energy $e = \varepsilon + \frac{1}{2}(u^2 + v^2)$ is the sum of the internal and kinetic energies. For a perfect or polytropic gas (Chap. 1 of Courant and Friedrichs [26]), the internal energy $\varepsilon = c_v T$, the enthalpy $h = \varepsilon + p/\rho = c_p T$, and the equation of state $p = \rho R T$, in which R and T denote the specific gas constant and gas temperature. The specific gas constant for argon follows as $R = \mathcal{R}/M = 208.132$ J/kg K, in which the universal gas constant $\mathcal{R} = 8,314.472$ kg/mol K and the molecular weight $M = 39.948$ kg/mol for argon. The specific heats at constant pressure and constant volume follow as $c_p = \gamma R/(\gamma - 1)$ and $c_v = R/(\gamma - 1)$. The specific heat ratio is given by $\gamma = c_p/c_v$ and taken as 5/3 for this study with monatomic argon.

A parallel, anisotropic, block-based adaptive mesh refinement (AMR) and finite-volume scheme using cells of regular- and irregular-shaped quadrilaterals is applied to the preceding set of partial differential equations and used to generate flow-field solutions by CFD for unsteady shock reflections from an inclined ramp. This numerical algorithm was developed over the past 13–15 years by Groth et al. [22,27–36] to solve challenging scientific and industrial problems involving unsteady flows with shock waves, internal ballistics of rocket motors, and premixed and non-premixed combustion flames. The stability and accuracy of the CFD solution algorithm, including the anisotropic AMR procedure [27,28,31,32], for producing high-resolution solutions of moving incident shock reflections from wedges were established previously by Hryniewicki et al. [27]. The CFD algorithm and solution details relevant directly to this paper are also well summarized earlier by Hryniewicki et al. [22],
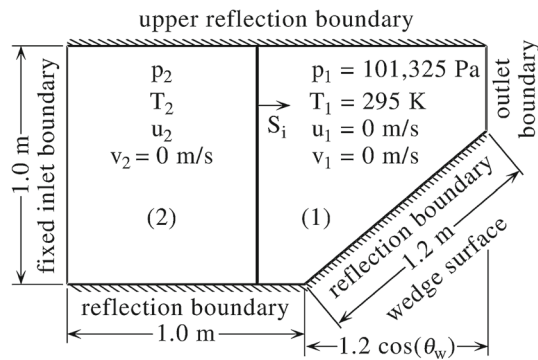
Fig. 4 CFD domain, boundaries, and initial conditions for flow-field simulations of shock reflections in argon using an inclined and rigid wedge with an angle θ_w

and these are described in more detail in the PhD thesis by Hryniewicki [37].

The computational domain, types of boundaries, and initial flow-field conditions ahead of the incident shock wave between regions (1) and (2) are shown in Fig. 4. The flow properties behind the incident shock front in region (2) are obtained from the shock-jump conditions of Rankine and Hugoniot [25]. The 1.2-m wedge-surface length allows the incident shock (projected downward to the wedge surface) to travel along the inclined wedge surface by 1 m for all flow-field simulations with incident shock Mach numbers from 1 to 4. The 1-m flow-field height and 1-m horizontal pre-wedge distance ensure that the shock reflected from the wedge does not contact the upper and left-hand boundaries during all CFD flow-field simulations. The wedge-surface length of 1.2 m was selected intentionally to be somewhat longer than the wedges used previously in most shock-tube experiments of shock reflections from straight wedges, for which the viscous effects are expected to be important and can influence the self-similar nature of RR and MR solutions.

The dynamic mesh adaptation from using the anisotropic AMR procedure is demonstrated in Fig. 5. The initial mesh at time zero consists of only two initial grid blocks depicted in Fig. 5a, and each grid block consists of a set of 8-by-8 cells that are not displayed. The left grid block is a square and exactly 1 m by 1 m as shown in Fig. 5a–d. The right grid block is of quadrilateral shape, 1 m high on the left side, $1.2\cos(\theta_w)$ m wide at the top, and squeezed into the space above the wedge. The shock discontinuity in Fig. 5a is shown by the vertical dashed line in the first block. Anisotropic AMR is implemented to refine the grid blocks around the shock discontinuity, before the numerical calculations begin, giving the results shown in Fig. 5b. During the computations, the shock reflection, flow field, and grid evolve, and the mesh changes to track and define complicated flow-field features (with large gradients in density and flow velocity), thereby helping to accurately compute flow-field features on a refined
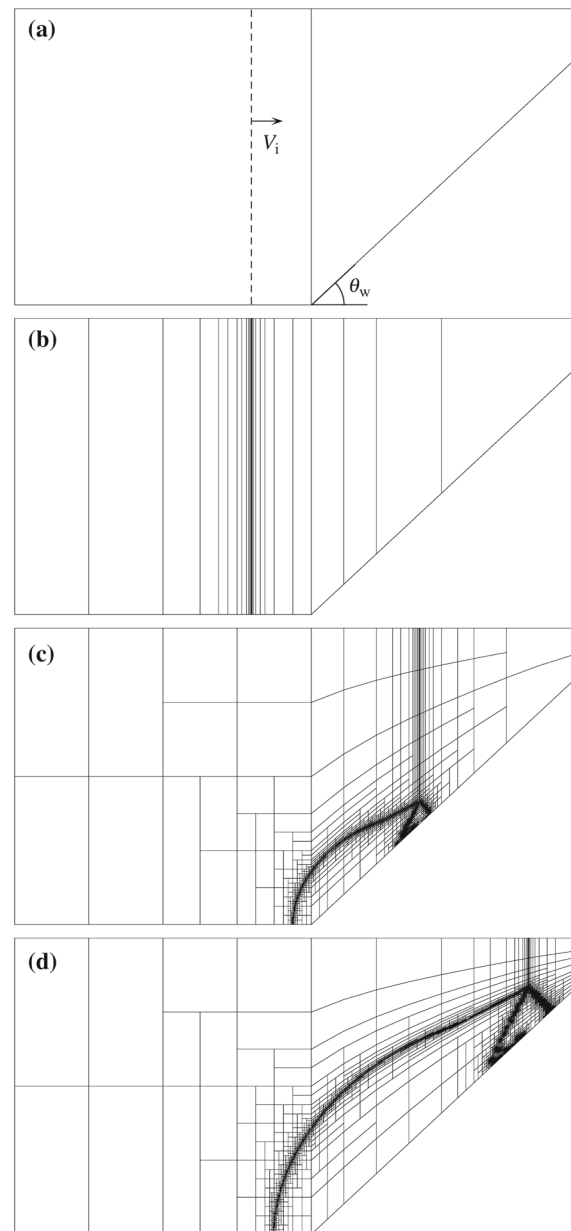

Fig. 5 Computational blocks at four stages of a TMR simulation in argon ($M_i = 4.0$ and $\theta_w = 43.0°$): **a** solution initialization, **b** initial anisotropic AMR application before CFD calculations begin, **c** early interaction of the incident shock with the wedge, and **d** later interaction

grid. Grid meshes are illustrated at early and late times in Fig. 5c and d, respectively, for a transitional-Mach reflection, as shown previously in Fig. 1c.

A square block with equal side lengths ℓ and 8-by-8 interior cells features initial cell-side lengths of $2^{-3}\ell$, for the first level of refinement. For n_r levels of refinement, the smallest cell-side lengths are reduced to $\delta = 2^{-n_r-3}\ell$. For $n_r = 12$, this corresponds to the smallest cell side of $\delta = 30.5\times10^{-6}\ell$, and a refinement factor of $\mathcal{R} = \delta/\ell = 2^{n_r+3}$ given by 32,768. The number of refinement levels is specified at the beginning

of each CFD flow-field simulation, and $n_r = 12$ was used most often in this study to generate flow-field simulations with high resolutions.

The reflection of planar shock waves from inclined wedges as predicted by Euler's equations is considered to be self-similar (theoretically). Therefore, the computed shock-reflected flow fields and wave patterns (i.e., RR, SMR, TMR, DMR) do not contain reference lengths. Hence, two computed flow fields and corresponding wave patterns for the case of a constant incident Mach number and wedge angle should be computed to the same accuracy when using two wedge lengths of 1 m and 2 m when the two uniform meshes contain N-by-N cells, respectively, where N is the number of cells in each x- and y-coordinate direction. In other words, separate computations of the same problem will yield flow-field solutions with about the same accuracy when N is the same for the 1-m and 2-m wedge lengths, or when the refinement factors $\mathcal{R} = \delta/\ell$ have about the same values. This information should be important for others to consider when attempting to reproduce the computational results reported later in this paper.

3 Numerical transition boundary between RR and MR based on near-field CFD data

3.1 Methodology and relevant results for argon

The extraction of the Mach-stem length (L) from each CFD flow-field simulation of either regular or Mach reflection is germane to the determination of whether the numerically computed pattern is RR ($L = 0$) or MR ($L > 0$). Furthermore, the determination of the transition boundary between RR and MR occurs when the Mach-stem length just approaches zero, so the accurate determination of small Mach-stem lengths, not easily discernible in magnified views of CFD flow-field images, is crucial. The Mach-stem length employed in this research is based on the Mach-stem offset length $L' = V_m \delta t - V_i \delta t / \cos(\theta_w)$ along the wedge, as shown in Fig. 6, in which V_i, V_m, δt, and θ_w denote the incident shock speed along the upper boundary (Fig. 4), Mach-stem speed along the wedge surface, time after the incident shock passes the wedge apex, and wedge angle, respectively. The time dependence of the dimensional length L' is removed by dividing it by $V_i \delta t / \cos(\theta_w)$, to obtain the normalized Mach-stem length,

$$L = \frac{V_m}{V_i} \cos(\theta_w) - 1, \tag{5}$$

which is constant for a self-similar flow. The triple-point trajectory angle χ (Fig. 6) is given correspondingly by
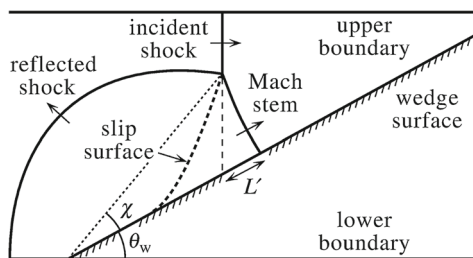

Fig. 6 Dimensional length L' of the forward displacement of the Mach stem, for the case of a single-Mach reflection

$$\tan(\chi) = \frac{V_m \cos(\theta_w) - V_i}{V_m \sin(\theta_w)} = \frac{1}{\tan(\theta_w)} \frac{L}{1+L}, \tag{6}$$

in terms of either the shock speeds V_i and V_m or the normalized length L. The accuracy of the computed values of L depends on the accuracy of determining the values of V_i and V_m from CFD flow-field simulations. Note that $V_m = V_i / \cos(\theta_w)$ theoretically for regular reflections, and then $L = 0$ and $\chi = 0°$ by (5) and (6), whereas $V_m = V_i \cos(\chi) / \cos(\theta_w + \chi)$ theoretically for Mach reflections with straight Mach stems normal to the wedge surface, and then $L > 0$ and $\chi > 0°$.

For monatomic gases like argon with $\gamma = 5/3$, as for diatomic gases and air with $\gamma = 7/5$ by Hryniewicki et al. [22], the determination of the numerical transition boundary for the range $1 < M_i \leq 4$ of incident shock Mach numbers is done at 20 locations along the extreme-angle boundary of von Neumann [1]. The selected reference points (RP) are shown graphically in Fig. 7 and tabulated numerically in Table 1.

At each reference point $(M_i^\star, \sin(\theta_w^\star))$ on the extreme-angle boundary, a set of coordinate points $(M_i, \sin(\theta_w))$ is specified for performing the CFD flow-field simulations, and these CFD points are marked by the sign "×", as illustrated at RP-6 and RP-15 in Fig. 7. A translated and rotated (α, β)-coordinate system is chosen with the α abscissa perpendicular and β ordinate parallel to the extreme-angle boundary so that the CFD flow-field simulations are chosen along a line perpendicular to the extreme-angle boundary. The CFD flow-field simulation points are calculated using

$$M_i = M_i^\star + \alpha \cos(\phi_w^\star) - \beta \sin(\phi_w^\star), \tag{7}$$

$$\sin(\theta_w) = \sin(\theta_w^\star) + \alpha \sin(\phi_w^\star) + \beta \cos(\phi_w^\star), \tag{8}$$

$$\phi_w^\star = \tan^{-1}\left(\frac{d \sin(\theta_w)}{d M_i}\bigg|_\star\right) - 90°, \tag{9}$$

with the parameter $\beta = 0$. The symbol $\phi_w^\star$ denotes the rotational angle of the (α, β)-axes, and $d[\sin(\theta_w)]/dM_i$ is the slope of the extreme-angle boundary. The selected CFD simulation points are concentrated in the vicinity of the
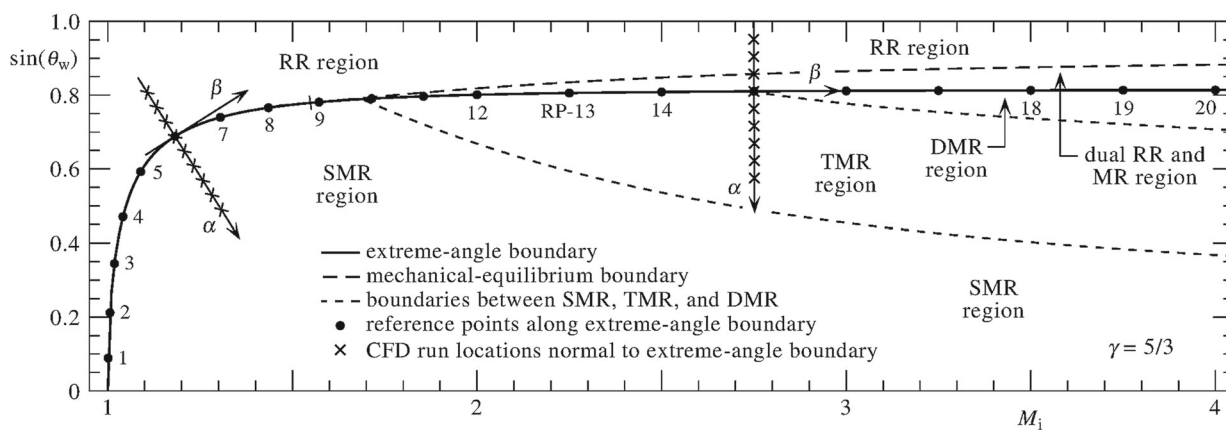
Fig. 7 Reference coordinates $(M_i^\star, \sin(\theta_w^\star))$ along von Neumann's extreme-angle boundary between RR and MR, and a superposed (α, β)-coordinate system showing the locations of CFD flow-field simulations perpendicular to this boundary

Table 1 Reference coordinates along the extreme-angle transition boundary for a monatomic gas ($\gamma = 5/3$)

RP	$M_i^\star$	$\theta_w^\star$ (°)	$\phi_w^\star$ (°)
1	1.001	5.1010	− 1.3040
2	1.006	12.2184	− 3.4760
3	1.018	20.1533	− 7.2071
4	1.041	28.0871	− 14.3370
5	1.089	36.3558	− 30.8163
6	1.182	43.4991	− 57.6984
7	1.305	47.7127	− 74.6128
8	1.435	49.9799	− 81.7594
9	1.572	51.3539	− 85.1728
10	1.715	52.2405	− 86.9823
11	1.855	52.8110	− 87.9754
12	2.0	53.2183	− 88.5968
13	2.25	53.6680	− 89.1901
14	2.5	53.9398	− 89.4949
15	2.75	54.1151	− 89.6662
16	3.0	54.2340	− 89.7690
17	3.25	54.3179	− 89.8342
18	3.5	54.3792	− 89.8773
19	3.75	54.4252	− 89.9068
20	4.0	54.4605	− 89.9276

Fig. 8 Continuous transitions of incident shock fronts in argon, constructed from curve fits to discrete CFD flow-field data, when the AMR level $n_r = 12$

numerical transition boundary by selecting values of the parameter α such that the Mach-stem length (L) just diminishes to zero in a set of very closely spaced or stationed Mach-reflection patterns.

The methodology of determining the incident shock and Mach-stem speeds to determine L and χ from (5) and (6) is long but well described in a previous work [22], so this description is not repeated. However, the most relevant incident and Mach-stem shock-front transitions, trajectories, and speeds for the specific case of monatomic argon are presented here for completeness.
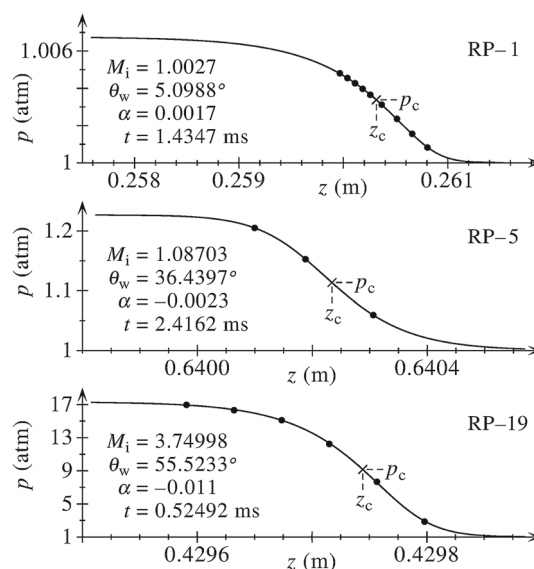
The incident shock front is spread over about three to twelve cells along the upper boundary (Fig. 4), as shown in Fig. 8, from CFD flow-field simulations at various time levels in the computations. The selection of these shock-front cells from a flow-field simulation, the curve fit to the data, and the extraction of the shock-front center location z_c at the center pressure p_c at each computational time (t_i) establishes the shock-front trajectory with time, $z_i = z_i(t_i)$, for each CFD flow-field simulation [22]. Sample results for the incident shock front are shown in Fig. 8 for RP-1, 5, and 19, at various values of the incident shock Mach number M_i, wedge angle θ_w, parameter α, and computational time t shown in the figure. These results have been computed with an adaptive mesh refinement (AMR) level $n_r = 12$, and they are typical of all incident shock fronts in argon constructed from CFD simulation data. The curve fit to the shock-front data
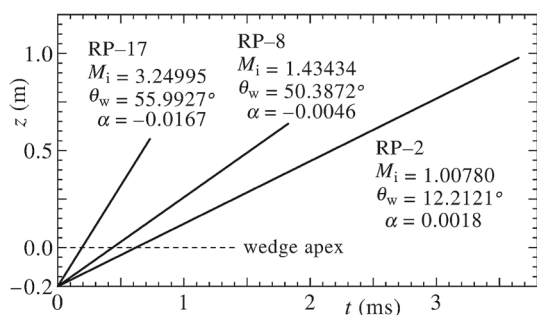
Fig. 9 Incident shock-front trajectories for argon as chains of $n = 8946$, 8376, and 8688 dots for RP-2, 8, and 17, respectively, when the AMR level $n_r = 12$

successfully captures the shock-front transition and provides an accurate center value of the shock-front transition to track the trajectory of the incident shock.

Three trajectories of the center of the incident shock front along the upper boundary are shown in Fig. 9 for RP-2, 8, and 17, with α values of 0.0018, -0.0046, and -0.0167, respectively. Each incident shock-front trajectory is plotted as a chain of numerous small dots. These shock-front trajectories for argon are typical of those for all reference points. A second-order polynomial given by $z = \bar{z}_i + \hat{a}(t - \bar{t}_i) + \hat{b}(t^2 - \bar{t_i^2})$ is fitted to the incident shock-front trajectories, for distances ranging from $z = 0.1$ m to the end of the computations at about $z_e = 1$ m. The overhead bar indicates an average (e.g., $\bar{t}_i = \frac{1}{n}\sum_{i=1}^{n} t_i$ for n data). The standard deviation of the incident shock trajectories, given by $\sigma_z = \overline{\{z(t_i) - z_i\}^2}^{1/2}$, was calculated. They are approximately $4\,\mu$m, which corresponds to determining the shock-front trajectory locations to about 1/8 of the size of the smallest cell sides of quadrilateral cells (for 12 levels of AMR). The trajectories look and are almost linear (coefficient $\hat{b} \approx 0$ m/s^2). The incident shock speed is given by $V_i = \hat{a} + 2\,\hat{b}\,t_e$, in which t_e is the time when the incident shock (projected downward on the wedge surface) has moved about 1 m along the wedge surface. For the trajectory data shown in Fig. 9 for RP-2, 8, and 17, the post-processing of the CFD simulations yielded incident shock-front speeds of 322.3984, 458.8673, and 1039.737 m/s. These computed values differ only slightly by 0.0019, 0.0016, and 0.0042 % from the corresponding theoretical values from the Rankine–Hugoniot equations for the incident shocks used to initialize the CFD flow-field simulations.

The Mach-stem shock front is also spread over about three to twelve cells along the wedge surface (Fig. 4), as shown in Fig. 10, from CFD flow-field simulations at various time levels of the computations. Sample results for this shock front are shown in Fig. 10 for RP-6, 11, and 14, for different values of M_i, θ_w, α, and t shown in the figure. These results are typical of all Mach-stem shock fronts in argon constructed from CFD simulation data. The curve fit to the shock-front
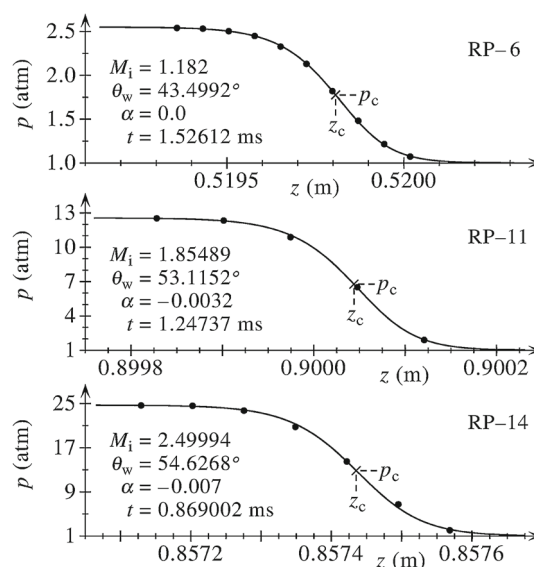

Fig. 10 Continuous transitions of reflected incident or Mach-stem shock fronts in argon, constructed from curve fits from discrete CFD flow-field data, when the AMR level $n_r = 12$

data successfully captures the Mach-stem shock-front transition and provides an accurate center value of the shock-front transition to track the trajectory of the Mach stem. What is considered here as the Mach-stem shock also includes either the coalesced incident and reflected shocks at the wedge surface for RR (with no Mach stem) or the obvious Mach-stem shock for MR (with a Mach stem).

Three composite trajectories of the center of the incident shock front along the lower horizontal pre-wedge boundary, and then the center of either the combined incident and reflected shock front for RR or the Mach-stem shock front for MR along the sloped wedge surface, are shown in Fig. 11 for RP-3, 8, and 17, for various values of M_i, θ_w, and α. These trajectories are kinked noticeably at the wedge apex location ($z = 0$ m), because the speed of the incident shock wave along the lower horizontal boundary before the wedge apex is slower than that of the shock traveling along the wedge surface. These shock-front trajectories for argon are typical of those obtained for all reference points.

A second-degree polynomial, $z = z(t)$, is fitted to the discrete trajectory data for the combined incident and reflected shocks (for RR from the wedge) or the Mach-stem shock (for MR), to determine the coefficients $\hat{a}$ and $\hat{b}$, as was done previously for the incident shock front. This curve fit is confined to shock-front data in the distance range 0.5 m $< z \le z_e$ along the wedge surface, where $z_e \approx 1$ m is the final shock-wave location near the end of the wedge. The curve fit is not as accurate as that for the incident shock because the standard deviations were roughly three to five times higher at about 15 μm (for 12 levels of AMR). This corresponds to determining the Mach-stem shock-front locations to about one
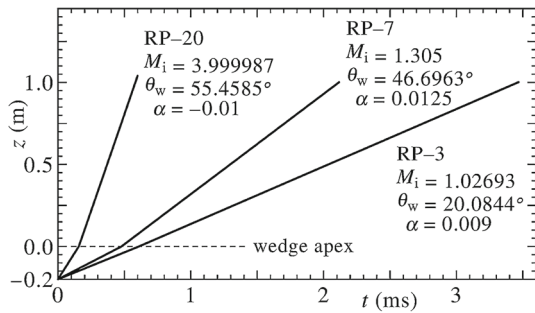
Fig. 11 Incident and Mach-stem shock-front trajectories for argon as a chain of 9537, 8509, and 9228 dots for RP-3, 7, and 20, respectively, when the AMR level $n_r = 12$

half the size of the smallest cells within the computed flow field with quadrilateral cells.

The speed of the shock front along the wedge surface, $V_m \approx V_i/\cos(\theta_w)$ for regular reflection (without a Mach stem), or $V_m \approx V_i \cos(\chi)/\cos(\theta_w + \chi)$ for Mach reflection (with a Mach stem), is calculated by differentiating the composite shock trajectory with respect to time. This shock speed is given by $V_m = \hat{a} + 2\hat{b}\,t_e$, where t_e is the time at the end of the flow-field simulation. These shock trajectories are not always linear for the specific case of the dual RR and MR region, so the full equation for V_m at the trajectory end when $z_e \approx 1$ m is used to determine V_m and calculate L and χ by (5) and (6). Note that the shock-front transitions and speeds for incident and Mach-stem shocks in Figs. 8, 9, 10 and 11 for monatomic gases like argon are similar in shape and linearity to those for diatomic gases and air [22], but the results differ numerically.

Five plots of the Mach-stem length L versus the parameter α (perpendicular to the extreme-angle boundary of von Neumann) are presented in Fig. 12 for RP-3, 7, 11, 15, and 18. Each plot shows the post-processed data from many closely spaced CFD flow-field simulations focused at and surrounding the numerical transition boundary (at which $L \rightarrow 0$). These near-field data that closely surround the numerical transition boundary are then used to determine this transition boundary accurately. This is done by determining the value of α_c at which L of MR patterns just diminishes to zero and the patterns then transcend into RR with $L \approx 0$.

The lower limits of the L versus α data (Fig. 12), when $L \rightarrow 0$ for MR results, are wide and bumpy for RP-1 to RP-8, which lie below the dual RR and MR region ($1 < M_i < 1.55$), whereas the bottoms are sharper but still bumpy for RP-9 to RP-20 associated with the dual RR and MR region ($M_i > 1.55$), as depicted in the selected 5 of the full 20 plots presented in Fig. 12. The start of larger bumpiness in the RR region of white filled circles (moving from left to right) by means of a few standard deviations from the average ($\bar{L}_{rr}$) is marked by the left-most vertical dashed line. The
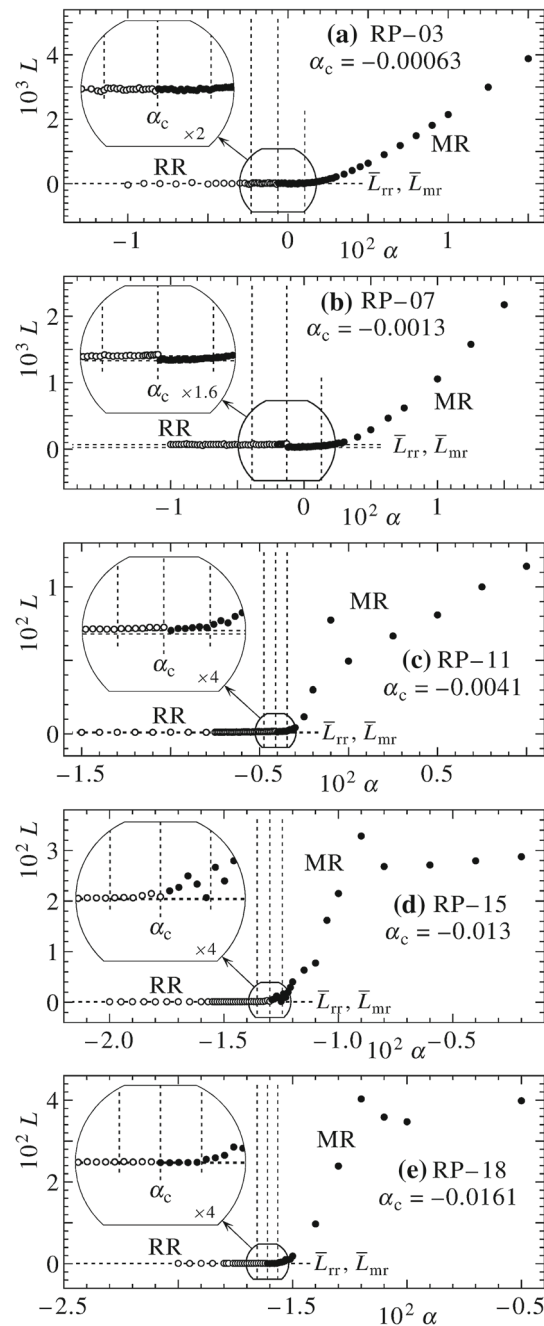

Fig. 12 Normalized Mach-stem length L versus parameter α for RP-3, 7, 11, 15, and 18, for the case of argon when the AMR level $n_r = 12$

beginning of large deviations in the MR region of black dots (also moving from left to right) by a few standard deviations from the average ($\bar{L}_{mr}$) is marked by the right-most vertical dashed line. These early and late indications of the transition between RR and MR are considered as bracketing the transition point between RR and MR. These marked locations are determined by using enlarged or magnified plots (factor of ten), whereas the enlargements shown in Fig. 12 are smaller

to make them fit into the diagrams. The transition value for α between RR and MR is then taken as the average of these early and late indicators, shown by the central vertical dashed line, and labeled as α_c. Although the transition boundary at α_c might appear to be known only approximately between the early and late markers, because of the magnification of and focus on the ($L \rightarrow 0$) region of the plot, this deviation is very small. The α variations on M_i and θ_w are typically less than 0.2%.

The rapid or abrupt RR-to-MR transition behavior shown in the plots in Fig. 12c–e in the dual RR and MR region is not a new phenomenon. This behavior associated with the dual region was noticed and explained in the late 1940s to mid-1950s, based on the observations of and questions about the experimental results reported by Smith[13], and based on theory and experimental-data interpretations of Bleakney and Taub[9] and Kawamura and Saito[10].

The numerical transition-boundary points between regular and Mach reflections from the post-processing of all of the CFD flow-field simulation data for the 20 reference points on von Neumann's extreme-angle transition boundary are summarized in Table 2. The values of the transition angle α_c, determined from the collection of near-field data with α values closely surrounding α_c (Fig. 12), and the corresponding

Table 2 Numerical transition boundary between RR and MR for an inclined wedge without a boundary layer in argon, based on near-field CFD data

RP	Reference points		Numerical transition points		
	$M_i^\star$	$\theta_w^\star$ (°)	α_c	M_i	θ_w (°)
1	1.001	5.1010	0.00022	1.00122	5.1007
2	1.006	12.2184	− 0.00060	1.00540	12.2206
3	1.018	20.1533	− 0.00063	1.01738	20.1581
4	1.041	28.0871	− 0.00020	1.04081	28.0903
5	1.089	36.3558	− 0.00050	1.08857	36.3741
6	1.182	43.4991	− 0.00110	1.18141	43.5726
7	1.305	47.7127	− 0.00130	1.30466	47.8195
8	1.435	49.9799	− 0.00080	1.43489	50.0505
9	1.572	51.3539	− 0.00080	1.57193	51.4271
10	1.715	52.2405	− 0.00270	1.71486	52.4935
11	1.855	52.8110	− 0.00410	1.85486	53.2012
12	2.0	53.2183	− 0.00670	1.99984	53.8641
13	2.25	53.6680	− 0.00945	2.24987	54.5920
14	2.5	53.9398	− 0.01160	2.49990	55.0847
15	2.75	54.1151	− 0.01300	2.74992	55.4060
16	3.0	54.2340	− 0.01460	2.99994	55.6911
17	3.25	54.3179	− 0.01510	3.24996	55.8291
18	3.5	54.3792	− 0.01610	3.49997	55.9950
19	3.75	54.4252	− 0.01625	3.74997	56.0583
20	4.0	54.4605	− 0.01640	3.99998	56.1106

incident shock Mach number M_i and wedge angle θ_w calculated using (7) and (8) are summarized as the new numerical transition boundary for argon in columns 4–6.

From the authors' present study with monatomic argon and subsequent to their previous study with diatomic gases and air [22], they have learned the following. In some cases for the computational results connected to the dual RR and MR region, the change from RR into MR along the wedge is delayed in the CFD computations, occurring farther along the wedge, because the smallest cells in the RR and MR patterns moving along the wedge actually get smaller from the wedge apex to the wedge end. This effect occurs because the second initial quadrilateral block and its subsequent subdivided quadrilateral blocks above the wedge are all tapered from the wedge apex toward the wedge end (as depicted in Fig. 5). Hence, the emergence of MR with extremely small Mach stems at the RR-to-MR transition boundary is not necessarily detected near the wedge apex in the computations, but the emergence of MR is often detected farther along the wedge when the smallest cells sizes in shock-wave patterns become even smaller. Once the smallest Mach reflections emerge farther along the wedge, even well past the middle of the wedge, they grow in size as the MR pattern moves along and toward the wedge end (1 m in the present computations), because the speed and size of the Mach-stem configuration require additional propagation space (e.g., larger than 0.5 m) and time to settle into a larger and possibly self-similar MR pattern. This delayed emergence of the Mach stem along the wedge means that the MR patterns with small Mach stems are not self-similar, with triple-point trajectories that are curved and do not start at the wedge apex, in contrast to what is expected from solutions of Euler's equations for inviscid flows. The computations of small non-self-similar MR patterns are considered affected by the minimum size of the quadrilateral cells and numerical viscosity in the authors' computational algorithm.

The computation of somewhat non-self-similar MR flow-field patterns that have small Mach stems, by solving Euler's equations for unsteady inviscid flows of shock interactions with a wedge, is not considered herein as detrimental to the authors' numerical determination of the RR-to-MR transition boundary. When computations produce Mach reflections with large Mach stems, the MR patterns are essentially self-similar, and these MR patterns obviously occur in the MR region, so they are also well below the RR-to-MR transition boundary that the authors are seeking to determine. When computations produce Mach reflections that have smaller and smaller Mach stems, these MR patterns do not grow initially in a self-similar manner (because the Mach-stem formations were delayed and the triple-point trajectory does not start at the wedge apex), but these results still lie in the MR region, but they are clearly closer and closer to the RR-to-MR transition boundary that is being sought. When subsequent

Fig. 13 Mach-stem length L versus parameter α for RP-5 and argon, when the AMR level $n_r = 10$, 11, 12, and 13
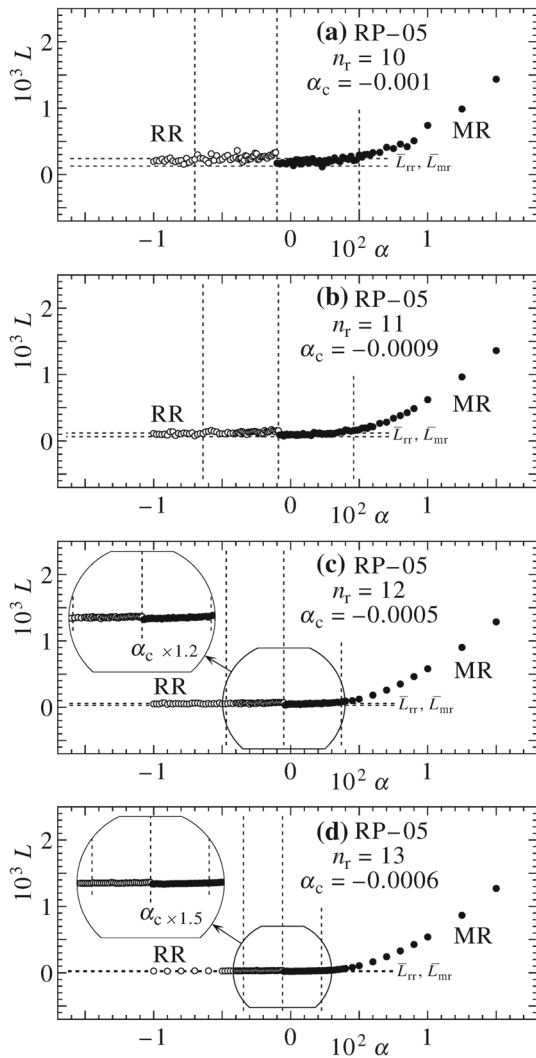
Fig. 14 Mach-stem length L versus parameter α for RP-16 and argon, when the AMR level $n_r = 10$, 11, 12, and 13

computations start to produce regular shock reflections, these reflections become essentially self-similar (and do not have Mach stems). These results must now lie in the RR region, so the RR-to-MR transition boundary must obviously have been passed. Hence, the RR-to-MR transition boundary must occur when the emergence of small Mach stems in computed wave patterns ceases from the MR patterns that are not self-similar, and self-similar RR patterns then occur in the RR region.

3.2 Study of mesh refinement on solution accuracy

The results of an investigation are reported herein for the evaluation of the effects of mesh refinement on improving the accuracy of CFD flow-field solutions and the subsequent post-processing determination of the new numerical transition boundary for argon separating regular and Mach
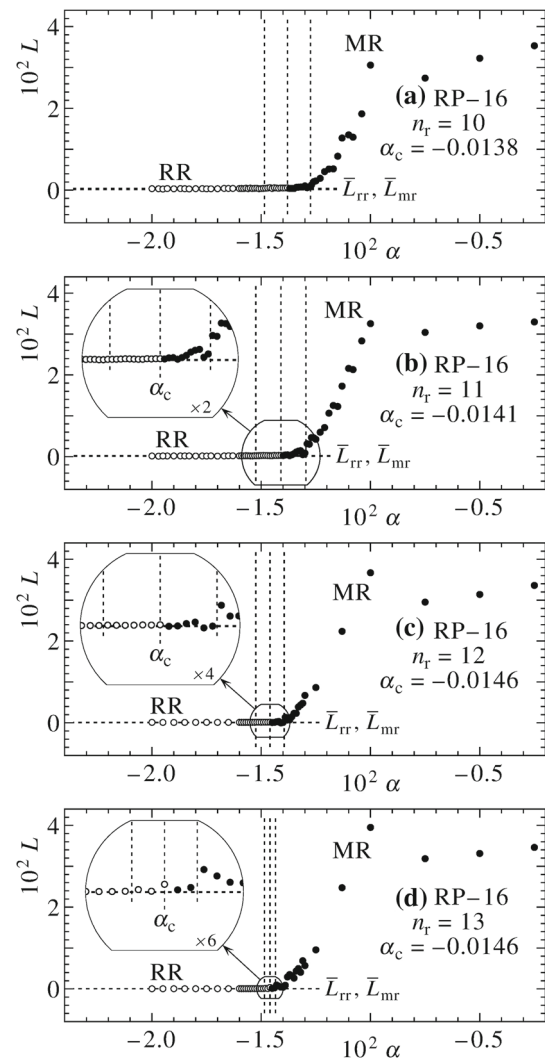
reflections. The objective is to demonstrate that the mesh was refined sufficiently well at 12 levels of anisotropic AMR such that the new results for the numerical transition boundary presented in Table 2, which came from CFD flow-field simulations, were well converged and grid independent so that this new numerical transition boundary can be considered reasonably accurate.

Four plots of the normalized Mach-stem length L versus the parameter α for AMR levels $n_r = 10$, 11, 12, and 13 are presented in Figs. 13 and 14 for reference points RP-5 and 16, respectively. The results for RP-5 are typical of all reference points for incident shock Mach numbers in the range $1.0 < M_i < 1.55$, for which the new numerical transition boundary agrees well with the closely spaced sonic and extreme-angle boundaries of von Neumann (Sect. 4). The results for RP-16 are typical of all reference points for incident shock Mach numbers in the range $1.55 < M_i < 4.0$, for

which the new numerical transition boundary trends above the closely spaced sonic and extreme-angle boundaries in the dual region of regular and Mach reflections (Sect. 4).

As the mesh is refined for AMR levels n_r from 10 to 13 for reference points RP-5 and 16 in Figs. 13 and 14, typical observations are given as follows: (1) the two averages $\overline{L}_{rr}$ and $\overline{L}_{mr}$ become more equal and converge toward the correct value of zero (most noticeable for RP-5), (2) the vertical variations in the data for regular reflection (white filled circles) diminish substantially (especially for RP-1 to 8), (3) the vertical variations in the data for Mach reflection (black dots) diminish more marginally, (4) the bottom transition region between regular and Mach reflections becomes narrower for RP-5 and sharper for RP-16, and (5) the early and late indicators of the emergence of a Mach stem, denoted by the two outer vertical dashed lines, contract for increasing levels of AMR. However, the average of these early and late indications, given by the center dashed line labeled α_c, shifts only slightly leftward (away from the sonic and extreme-angle boundaries), less and less as the value of α_c converges to a nearly constant value. Note that the accuracy of the post-processed L versus α results is generally better for stronger incident shocks ($M_i > 1.55$) within the dual region of regular and Mach reflections than it is for weaker incident shocks ($1.0 < M_i < 1.55$) before the dual region. For instance, this is evident from a comparison of the transition profiles of RP-16 with those of RP-5 for a given AMR level in Figs. 13 and 14.

The small changes in the transition values of α_c with increasing mesh refinement, as can be seen in Figs. 13 and 14 for reference points RP-5 and 16 with AMR levels $n_r = 10$ to 13, are not significant in changing the numerically determined transition-boundary points (M_i, θ_w) presented earlier in Table 2. If the early and late vertical dashed line indicators of the emergence of the Mach stem in the plots of L versus α are considered as error bars on the transition value of α_c, then the results shown in Table 2 for M_i and θ_w are accurate in the worst cases to within $\pm 0.33\%$ and $\pm 0.47\%$, for all 20 reference points selected along von Neumann's extreme-angle transition boundary. The resulting error bars would not be noticeable if they were placed on the symbols used to plot the incident shock Mach number M_i versus the wedge angle θ_w for the numerically determined transition points (like data shown in Figs. 2 and 3), because these error bars would each be covered entirely by the white filled circle and black dot markers.

Based on the preceding and other similar studies, the use of 12 levels of AMR is considered sufficient to accurately determine the new transition boundary separating regular and Mach reflections in this research. This conclusion is based on the present mesh refinement study on CFD solution accuracy, in conjunction with the preceding results for determining the incident shock and Mach-stem speeds V_i

and V_m in Sect. 3.1 that illustrate the high accuracy of the post-processing methodology in the computations of the incident and Mach-stem shock speeds V_i and V_m used in the calculations of the Mach-stem length L. At the mesh resolution of 12 levels of AMR, the predicted CFD flow-field solutions and post-processed transition-boundary points are considered essentially independent of the mesh densities used in the CFD flow-field simulations.

4 Numerical transition boundary between RR and MR based on far-field CFD data

Plots of the normalized Mach-stem length L versus the parameter α (perpendicular to the extreme-angle boundary), such as those presented previously in Fig. 12 for argon, are replotted differently here by using the triple-point angle χ versus α. Four plots of these alternate representations of the data for determining the transition boundary between regular and Mach reflections are presented in Fig. 15 for reference points RP-13, 15, 18, and 20, with reference incident
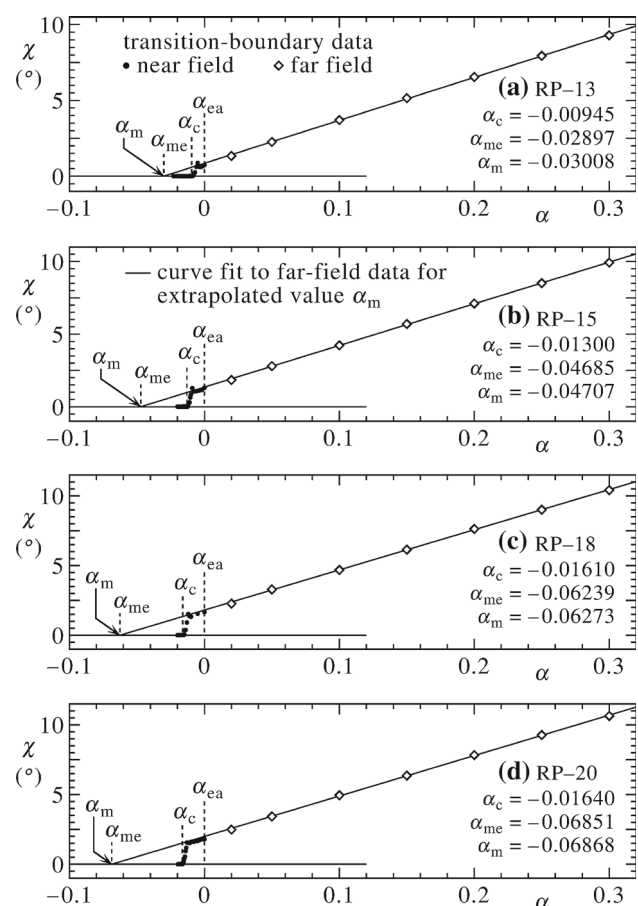

Fig. 15 Three possible transition boundaries between RR and MR in argon given by the locations α_{ea}, α_c, and α_m or α_{me}

shock Mach numbers $M_i^\star = 2.25, 2.75, 3.5$, and 4.0, respectively. These plots for the variation in χ versus α correspond to incident shock Mach numbers that lie within the range $1.55 < M_i < 4$ for the dual RR and MR region (Fig. 2).

The post-processed data for χ versus α from CFD flow-field simulations of regular and Mach reflections in argon are subdivided into two groups in Fig. 15. The first group of closely spaced near-field data, included as the collection of black dots, was used previously in Sect. 3 to determine the new numerical transition boundary between regular and Mach reflections (without a boundary layer on the wedge surface), yielding the values of α_c given in Table 2 for argon. The location of α_c occurs when the normalized length L and the triple-point angle χ both just diminish to zero for the transition from Mach to regular reflection. The location of α_c among these closely spaced near-field data is shown by a vertical dashed line labeled α_c in each plot in Fig. 15.

The location of the transition boundary between regular and Mach reflections from von Neumann [1], based on the extreme-angle or detachment criterion, is also shown in each plot as a vertical dashed line labeled α_{ea}. This location occurs exactly at the point $\alpha = 0$, which stems from the definition of α that is centered on and runs perpendicular to the extreme-angle boundary. Based on the data shown in Fig. 15 for the dual region of regular and Mach reflection, von Neumann's transition boundary is not valid for inviscid flows (without a boundary layer on the wedge), because the CFD flow-field simulations do not feature both L and χ equal to zero at the location α_{ea} in the dual region. Nonetheless, the closely spaced sonic boundary (not shown) and extreme-angle boundary in the dual region can be considered as being relatively close to the new numerical transition boundary, making these sonic and extreme-angle boundary estimates rather respectable, considering that they are based on relatively simple analytical predictions using the assumption that the incident shock, reflected shock, Mach stem, and slip stream are all linear or straight lines.

The second group of post-processed data for χ versus α is shown as a distributed set of white filled diamonds in Fig. 15. This group of data is called far-field data, partly because these data do not surround the transition-boundary location α_c between regular and Mach reflections, partly because they do not surround the nearby boundary location α_{ea} stemming from von Neumann's extreme-angle criterion, and partly because the triple-point angles and Mach-stem lengths in these Mach-reflection patterns are rather large and atypical of those that should occur close to a RR-to-MR transition boundary. The straight line in each plot in Fig. 15 is produced by a least-squares curve fit to the far-field data only (data with diamond symbols). The extrapolation of the straight line of χ versus α to $\chi = 0$ yields the value of α labeled α_m in each plot in Fig. 15. The extrapolated values given by α_m lie very

Table 3 Numerical transition boundary between RR and MR using extrapolated far-field data for argon

RP	Reference points		Numerical transition points		
	$M_i^\star$	$\theta_w^\star$ (°)	α_m	M_i	θ_w (°)
9	1.572	51.3539	0.00348	1.57229	51.0369
10	1.715	52.2405	− 0.00446	1.71477	52.6589
11	1.855	52.8110	− 0.01177	1.85458	53.9410
12	2.0	53.2183	− 0.01930	1.99953	55.1063
13	2.25	53.6680	− 0.03008	2.24958	56.6859
14	2.5	53.9398	− 0.03918	2.49966	57.9496
15	2.75	54.1151	− 0.04707	2.74973	59.0111
16	3.0	54.2340	− 0.05273	2.99979	59.7842
17	3.25	54.3179	− 0.05787	3.24983	60.4744
18	3.5	54.3792	− 0.06273	3.49987	61.1186
19	3.75	54.4252	− 0.06388	3.74990	61.3105
20	4.0	54.4605	− 0.06868	3.99991	61.9330

close to the mechanical-equilibrium boundary, which is also shown using the symbol α_{me} in the four diagrams in Fig. 15 for direct comparisons.

Each value of α_m and the corresponding incident shock Mach number M_i provide a possible transition-boundary point separating regular and Mach reflections for the dual region ($M_i > 1.55$). These particular extrapolated transition-boundary points have the correct results that $\chi = 0°$ and $L = 0$. However, these extrapolations of far-field Mach-reflection data pass over the new numerical transition boundary, and also over most or all of the remaining dual region, and lie on or close to the mechanical-equilibrium boundary. Therefore, these extrapolated boundary points occur where CFD flow-field simulations yield only flow-field solutions corresponding to RR patterns, because $\alpha < \alpha_c$. Hence, this supposedly RR-to-MR transition boundary cannot be correct, because Mach reflections with Mach stems do not occur up against one side of this boundary. Hence, the extrapolated results of far-field data (χ versus α in Fig. 15) yield an incorrect and misleading RR-to-MR transition boundary.

These numerical transition-boundary points from post-processing only CFD far-field data for reference points RP-9 to 20 to obtain the extrapolated values for α_m are nonetheless collected in column 4 of Table 3. The corresponding incident shock Mach numbers M_i and wedge angles θ_w, calculated using (7) and (8), are listed in columns 5 and 6. These data facilitate the discussion and conclusions presented in Sect. 5.2.

5 Final discussion and conclusions

The final discussion and main conclusions are organized into the three subsections that follow, based on the stated three primary objectives of this study.

5.1 Transition boundary between RR and MR using near-field data

The regions of and transition boundaries between regular and Mach reflections (i.e., RR, SMR, TMR, and DMR) from wedges in argon are presented in Fig. 16, in a plot of the wedge angle θ_w versus the incident shock Mach number M_i. The new numerical transition boundary between regular and Mach reflections in argon, which was determined from CFD field-flow simulations (inviscid flows) using near-field data, for the case of no boundary layer on the wedge surface, is defined by the string of 20 white filled circles. These data were taken directly from Table 2.
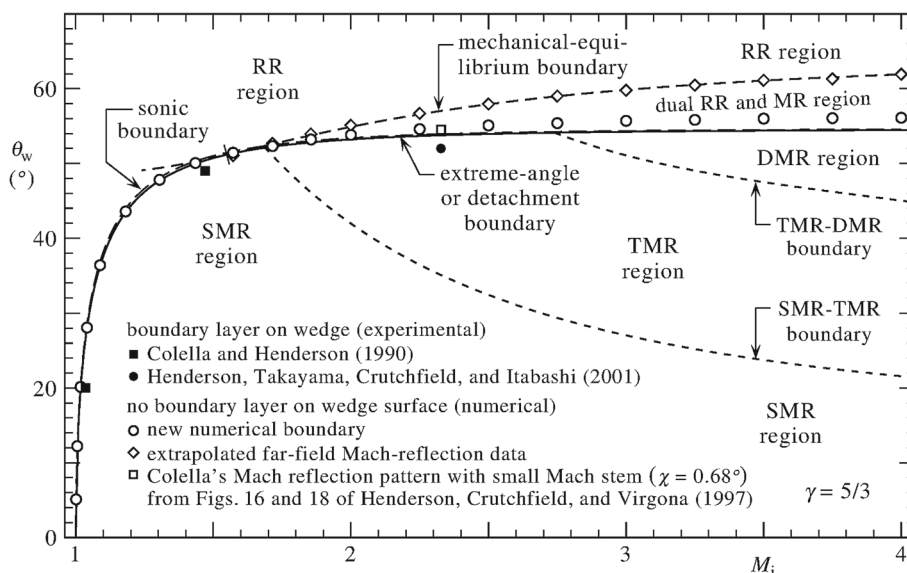
The numerical transition boundary between regular reflection and Mach reflection (SMR, TMR, and DMR) in argon is in good agreement with the extreme-angle or detachment boundary of von Neumann [1] for lower incident shock Mach numbers in the range $1 < M_i < 1.55$, corresponding to those below the dual RR and MR region. This transition boundary then deviates above the closely spaced sonic and extreme-angle boundaries by about two degrees for larger Mach numbers in the range $M_i > 1.55$, corresponding to those of the dual RR and MR region. This upward trend at larger incident shock Mach numbers is noticeable, increases continuously without fluctuations, and is significant in that it trends higher than the sonic and extreme-angle boundaries of von Neumann by as much as two degrees. This behavior is very similar in trend to that for the numerical transition boundary for diatomic gases and air, as shown earlier in Fig. 3. Hence, the behavior or trend (but not numerical values) is the same for diatomic and monatomic gases even though the specific heat ratio changes from $\gamma = 7/5$ to $5/3$, respectively.

The behavior or trends for both monatomic and diatomic gases, illustrating the effects of changing the specific heat ratio γ from 5/3 to 7/5, are shown in Fig. 17. The additional extreme-angle and mechanical-equilibrium boundaries for the case of $\gamma = 1.09$ for sulfur hexafluoride (as a polytropic gas) are included for comparison. All experimental data for both argon and air shown previously in Figs. 2 and 3, respectively, are included in Fig. 17 for completeness and interest. Although the trends for different types of gases are similar, the corresponding transition boundaries and experimental data differ significantly in location in the plot of wedge angle versus incident shock Mach number.

Although the numerical transition boundaries between regular and Mach reflections for monatomic gases like argon and diatomic gases and air are in good agreement with the closely spaced sonic and extreme-angle boundaries for low incident shock Mach numbers ($1 < M_i < 1.55$), the results for the numerical transition boundary in this Mach number range are not sufficiently accurate to provide a definitive conclusion as to whether they agree better with the sonic or extreme-angle boundary, because the sonic and extreme-angle boundaries lie so close together and the numerical data are not sufficiently accurate for this situation.

The three experimental data (black markers) shown in Fig. 16 interpreted from the papers by Colella and Henderson [6] and Henderson et al. [11] for the case of moving incident shock reflections from an inclined wedge with a combined thermal and viscous boundary layer in argon, lie below the extreme-angle or detachment boundary by about a couple of degrees. These sparse data imply that, for the case of viscous flow with a boundary layer on the wedge surface, the RR-to-MR transition boundary lies below the new numerical boundary and von Neumann's closely spaced sonic and extreme-angle boundaries. This implication is much more

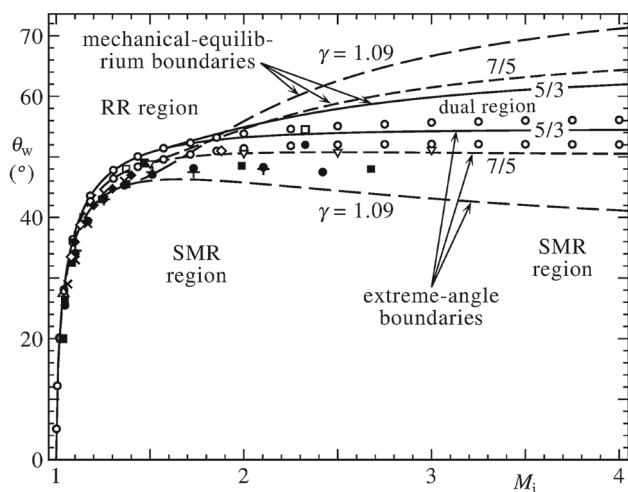**Fig. 16** Regions and transition boundaries separating regular and Mach reflections for an inclined wedge in argon

Fig. 17 Effects of varying the specific heat ratio (γ) on the extreme-angle, mechanical-equilibrium, and numerical transition boundaries for monatomic gases like argon, diatomic gases and air, and sulfur hexafluoride (SF_6) with $\gamma = 1.09$

evident for the case of the reflection of moving shocks from wedges in diatomic gases and air (as introduced earlier in Fig. 3), because the experimental data are more plentiful and thereby yield a more recognizable moderately wide-banded experimental transition boundary.

The downward shifts by as much as three degrees from the numerical transition boundaries in argon and air without a boundary layer (inviscid) down to the experimental data with a boundary layer (viscous), as shown in Figs. 16 and 3, respectively, illustrate the importance of the thermal-conductivity and viscous-flow effects associated with the boundary layer on the wedge surface. Regular reflections with a boundary layer on the wedge surface persist downward across the entire dual RR and MR region, including the numerical transition boundary and closely spaced sonic and extreme-angle boundaries, slightly into the Mach-reflection region (SMR, TMR, and DMR). Alternately, Mach reflections without a boundary layer on the wedge surface persist upward from the Mach reflection region into the dual RR and MR region, across the closely spaced sonic and extreme-angle boundaries, and terminate at the new numerical transition boundary inside the dual region. The current images of CFD flow-field simulations without a boundary layer on the wedge surface are always regular-reflection patterns for the region between the numerical transition boundary and the higher mechanical-equilibrium transition boundary of von Neumann. This well illustrates that the mechanical-equilibrium boundary is not appropriate to consider as the transition boundary between RR and MR for the reflection of a moving incident shock from a wedge. Most of these conclusions were presented earlier in the experimental and numerical paper by Henderson et al. [11], for shock reflections without and with a wedge with a boundary layer in

argon, but the MR-to-RR transition for the case of inviscid flow was mentioned as occurring close to but slightly above the extreme-angle or detachment transition boundary, which would likely occur near the new numerical RR-to-MR transition boundary presented herein.

Good support for the new numerical transition boundary for argon for the case of no boundary layer on the wedge surface by means of shock-tube experiments in argon is not available. However, the publication of the present results might stimulate some researchers to make experimental measurements, using one of the types of shock-tube facilities reviewed in Sect. 5 of the paper by Hryniewicki et al. [22], to either confirm or reject the numerical transition boundary separating regular and Mach reflections.

Support for the new numerical transition boundary for argon without a boundary layer on the wedge surface by means of CFD studies from other researchers is also scarce. The work of Henderson et al. [24] contains one result of a CFD flow-field simulation that supports the authors' new numerical transition boundary for argon. This result is shown graphically in their Figs. 16 and 18 for a CFD flow-field simulation done for a shock Mach number $M_i = 2.327$ and wedge angle $\theta_w = 54.5°$ (taken from their figures). The flow-field pattern that lies above the extreme-angle boundary must be that of a Mach reflection, because it has a small triple-point angle of $0.68°$ (also from their figures), which corresponds to a normalized Mach-stem length $L = 0.017$ calculated by means of (5). The CFD flow-field calculations for inviscid flows were mentioned as being completed by Phillip Colella, at the end of their conclusions, as part of some of his earlier studies, possibly from part of Colella and Henderson's research for their paper [6], although the data were not reported therein.

The flow-field computation of Colella for $M_i = 2.327$ and $\theta_w = 54.5°$ in argon is shown as the white filled box in Fig. 16, for the case of inviscid flow and no boundary layer on the wedge surface. This Mach-reflection point lies $0.68°$ above the extreme-angle boundary, and it has a small Mach stem, so the actual transition boundary between MR and RR should lie above Colella's result, which would obviously be very close to the authors' numerical transition boundary. Consequently, this flow-field computation of Colella is considered here as providing some conclusive support for and verification of the new numerical transition boundary.

The physical mechanism or reasons for the upward shift in the authors' numerical transition boundary, above von Neumann's closely spaced sonic and extreme-angle transition boundaries, within the dual region of regular and Mach reflections, are not yet completely understood for both cases of monatomic gases like argon and diatomic gases and air. This upward shift inside the dual region is not believed to stem from numerical or flow disturbances, or from modeling errors in the CFD computations. The string of 20 white filled circles

Table 4 Regular and Mach reflections when $1 < M_i < 1.55$ (below the dual RR and MR region)

θ_w range	Without boundary layer	With boundary layer
$0° < \theta_w < [\theta_{exp}^i \approx \theta_{ea} \approx \theta_n \approx \theta_s]$	MR[a]	
$[\theta_{exp}^i \approx \theta_{ea} \approx \theta_n \approx \theta_s] < \theta_w < 90°$	RR	
$0° < \theta_w < \theta_{exp}^v$		MR[a]
$\theta_{exp}^v < \theta_w < \theta_{ea}$		RR
$\theta_{ea} < \theta_w < \theta_s$		RR
$\theta_s < \theta_w < \theta_n$		RR
$\theta_n < \theta_w < 90°$		RR

[a] MR is either SMR or vNR

Table 5 Regular and Mach reflections when $M_i > 1.55$ (within the dual RR and MR region)

θ_w range	Without boundary layer	With boundary layer
$0° < \theta_w < \theta_{exp}^v$	MR[a]	MR[a]
$\theta_{exp}^v < \theta_w < \theta_{ea}$	MR[a]	RR
$\theta_{ea} < \theta_w < \theta_s$	MR[a]	RR
$\theta_s < \theta_w < \theta_n \approx \theta_{exp}^i$	MR[a]	RR
$\theta_n \approx \theta_{exp}^i < \theta_w < \theta_{me}$	RR	RR
$\theta_{me} < \theta_w < 90°$	RR	RR

[a] MR is either SMR, TMR, or DMR

is neither erratic nor jerky in behavior. Instead, they occur in a uniform and systematic manner, as shown in Fig. 16. The numerical transition boundary is generated by high-resolution CFD flow-field simulations, which fully account for the shock-reflection process from the inclined wedge. The effects of the entire corner wave are included fully in these computations, as are those of the curved reflected shock when the corner wave overtakes the incident shock in RR and the triple point in MR. Consequently, it should not be expected that the new numerical transition boundary will agree well with the sonic and extreme-angle boundaries for both small and large Mach numbers. Von Neumann's two transition boundaries, based on his sonic and extreme-angle criteria, originate from fairly simple analytical considerations in which the incident, reflected and Mach-stem shocks, and the slip stream are all assumed planar or straight. Moreover, von Neumann's analytical derivations ignore the entire corner wave for the extreme-angle boundary and take the speed of this wave into account only for the sonic transition boundary [22]. The reasons for the unexpected shift in the numerical transition boundary upward into the dual RR and MR region are currently being investigated.

As a recap, the occurrences of regular and/or Mach reflection in various ranges of the wedge angle θ_w, for inviscid argon flows without a boundary layer and thermal and viscous flows with a boundary layer on the ramp surface, are summarized in Tables 4 and 5. These tables pertain to incident shock Mach numbers in the range $1 < M_i < 1.55$ prior to the dual RR and MR region, and for $M_i > 1.55$ within the dual region. In these tables, the symbols θ_{ea}, θ_s, θ_n, and θ_{me} denote the respective wedge angles for the extreme-angle, sonic, new numerical, and mechanical-equilibrium transition boundaries. Also, θ_{exp}^i and θ_{exp}^v denote the transition boundary from the string of experimental results without and with a combined thermal and viscous boundary layer on the wedge, corresponding to inviscid and viscous flows, respectively.

5.2 Transition boundary between RR and MR using far-field data

A possible alternate transition boundary between regular and Mach reflections from inclined wedges without a boundary layer in argon for the dual RR and MR region ($M_i > 1.55$) is produced in Sect. 4 and collected in Table 3. These tabulated data were obtained from Mach-reflection configurations with relatively large Mach stems and triple-point angles, and the alternative transition boundary was determined by linear extrapolation of these far-field data for χ versus α to $\chi = 0°$, to obtain the transition-boundary value of α_m, from which the corresponding values of M_i and θ_w were obtained. These extrapolated results are shown in Fig. 16 as the twelve white filled diamonds. The locations of the plotted data are surprising in that they lie on or very close to the mechanical-equilibrium boundary of von Neumann [1]. These extrapolated locations provide a powerful suggestion that the mechanical-equilibrium boundary is the transition boundary between RR and MR, especially if one is unsure where the transition boundary lies, and more so if one also
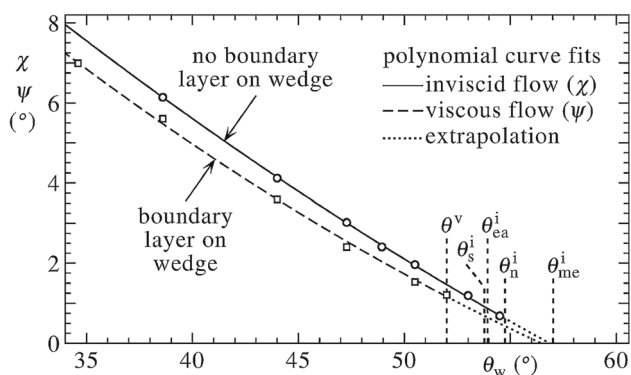
Fig. 18 Quadratic polynomial extrapolations of argon data by Henderson et al. [24] to determine the transition-boundary wedge angle θ_w at $M_i = 2.327$ between RR and MR from a wedge, without and with a boundary layer on the wedge surface

does not know that the RR-to-MR transition occurs as a rapid or an abrupt change in shock-front properties for the dual RR and MR region.

The mechanical-equilibrium boundary, however, is not a valid transition boundary for the change from regular to Mach reflection in the dual region, as mentioned previously in Sect. 4. The extrapolation of far-field data simply overshoots the new numerical boundary at which the transition from RR to MR occurs as a very rapid or abrupt change in the flow properties (including χ). This was first discovered in 1949 by Bleakney and Taub [9], concerning the experimental data of Smith [13], and studied further and confirmed in 1956 by a different but complementary study of Kawamura and Saito [10].

One example of extrapolating far-field MR data and concluding incorrectly that the RR-to-MR transition boundary is the mechanical-equilibrium boundary was done by Henderson et al. [24], for the case of shock reflections from a wedge without and with a boundary layer on the wedge surface in argon. Their results (in Fig. 18) are included in the authors' revised Fig. 18 herein to facilitate the discussion. The symbols χ and ψ denote the usual and self-similar triple-point angles for numerical experiments using the Euler and Navier–Stokes equations for inviscid and viscous flows, respectively, with ψ being corrected for parallax error associated with viscous flows. The extreme-angle, sonic, and mechanical-equilibrium boundaries of von Neumann are included at the wedge angles given by $\theta_{ea}^i = 53.776°$, $\theta_s^i = 53.924°$, and $\theta_{me}^i = 57.021°$, respectively, whereas $\theta_n^i = 54.744°$ is the numerical transition boundary of the present authors, and all correspond to inviscid flows without a boundary layer on the wedge surface. The symbol $\theta^v = \theta_w^v = 52°$ is the transition boundary between RR and MR for a 0.17-m-long wedge with a boundary layer on the wedge surface, which is shown in Figs. 2 and 16. The origin of this transition-boundary wedge

angle of $\theta^v = 52°$ from Henderson et al. [11] is explained in Sect. 1. Colella's flow-field simulation at $\chi = 0.68°$ and $\theta_w = 54.5°$, mentioned earlier and plotted in Fig. 16, is now also shown in Fig. 18, beyond the extreme-angle boundary (θ_{ea}^i) and just before or below but very close to the authors' numerical transition boundary (θ_n^i).

The conjectures made by Henderson et al. [24], based on their quadratic extrapolations of far-field data, that the transition boundary separating RR and MR for both inviscid and viscous flows is the mechanical-equilibrium boundary were incorrect and misleading. However, such conjectures were not continued in the subsequent paper by Henderson et al. [11].

5.3 Significance of computed transition boundary between RR and MR for inviscid flow reflections

Consider regular reflection from an inclined wedge with a boundary layer on the wedge surface, as sketched in Fig. 19. The size of the regular-reflection pattern is characterized by a simple overall length denoted by the distance z, but the size of the boundary layer characterized by its length and thickness is more complicated, because the boundary layer consists of two separate parts. One part is produced by the incident and reflected shocks joined together at the wedge surface and moving together along this surface. This shock-induced boundary-layer flow extends from its front at the joined shocks backward down the wedge toward the apex by a length denoted as z_{si}. If a single-Mach-reflection pattern is used to illustrate this first type of boundary layer, then it will extend backward from the Mach-stem shock to the point at which the slip stream touches the wedge surface, because all of the pre-Mach-stem gas engulfed by the Mach stem during its motion along the wedge resides within the moving triangular region consisting of the Mach stem, slip stream, and wedge surface.
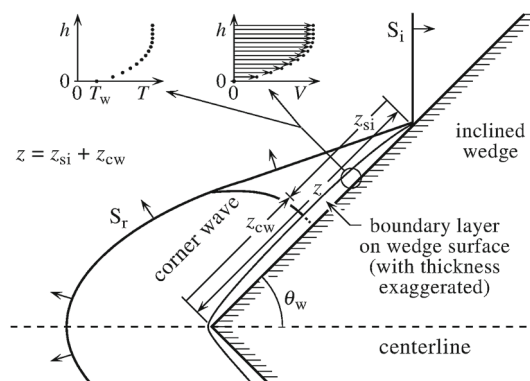

Fig. 19 Regular reflection with a boundary layer on the wedge surface, the boundary-layer temperature and flow-velocity variations, and the length of the reflection pattern in terms of the two boundary-layer lengths

The other part of the boundary layer on the wedge surface in Fig. 19 is produced differently by the flow behind the reflected shock near the central plane. Although the oncoming incident shock induces an initial flow toward the wedge, this flow also passes through the reflected shock that moves leftward and is slowed in its movement rightward. This rightward moving slowed flow near the centerline impacts the front of the wedge, and it then moves along the wedge surface as part of the corner wave, producing this second boundary layer of length denoted by z_{cw}. The front of this boundary layer is at or near the wedge apex, which is detached from the apex because of the flow stagnation point at the apex. This flow stagnation can be observed in each CFD flow-field velocity image of RR, SMR, TMR, and DMR shown in Fig. 1. The combined length of these two boundary layers, each facing the opposite direction and abutting somewhere along the wedge surface (between the incident shock and wedge apex), is the overall wave-pattern length z. Hence, $z = z_{si} + z_{cw}$.

Becker[38] provided a detailed treatment of shock-induced boundary layers, and Hornung and Taylor[39] and Hornung[40] have applied Becker's work to determine the effects of the shock-induced boundary layer on both the transition boundary from RR to MR and the Mach-stem height. From Becker and Hornung's papers, the displacement thickness δ^* of the shock-induced boundary layer on the wedge can be expressed as

$$\delta^* = -F\big[M, \gamma, \text{Pr}, T_w/T_o\big] x \left[\frac{\ell_v}{x}\right]^{1/2} \quad (10)$$

for laminar flow. The function F is evaluated from local flow conditions just outside and near the front of the boundary layer, in terms of the flow Mach number M, specific heat ratio γ, Prandtl number Pr, and ratio of the wall temperature T_w to the stagnation-flow temperature T_o. The viscous length $\ell_v = \mu/(\rho V)$ is also evaluated from local conditions and depends on the dynamic viscosity μ, gas density ρ, and flow speed V along the wedge. The distance x is measured from the front of the boundary layer along the wedge surface, that is backward down the wedge for the shock-induced boundary layer, and forward up the wedge for the other boundary layer induced by the flow up the wedge (as part of the corner wave).

The shock-induced boundary-layer thickness δ_{si}^* at the location $x = z_{si}$, possibly halfway back down the wedge surface toward the apex, can be rewritten as

$$\frac{\delta_{si}^*}{z} = -F\left[\frac{z_{si}}{z}\right]^{1/2}\left[\frac{\ell_v}{z}\right]^{1/2} = -F\left[\frac{z_{si}}{z}\right]^{1/2} \text{Re}_z^{-1/2}, \quad (11)$$

for the case of laminar flow. The Reynolds number is defined as $\text{Re}_z = z/\ell_v = \rho V z/\mu$, based on the overall shock-reflection length z. The function F and viscous length ℓ_v should be reasonably constant for a particular regular-reflection pattern for a constant incident shock Mach number, as the pattern grows in size with time during the expanding shock-reflection process from the wedge. Furthermore, the length ratio z_{si}/z should be reasonably constant in the expanding shock-reflection pattern with time. Therefore, the boundary-layer length ratio δ_{si}^*/z will diminish with $(\ell_v/z)^{1/2}$ or $\text{Re}_z^{-1/2}$ as z increases with increasing time, as the shock-reflection pattern expands in size. This illustrates clearly that the reflected shock pattern grows more quickly with time than the thickness of the shock-induced boundary layer, and this growth difference is incorporated in the Reynolds number Re_z, which is based by selection on the shock-reflection pattern length z.

The Reynolds number is approximately zero when the shock-reflection pattern just emerges or forms at the wedge apex, so the boundary-layer thickness is relatively large compared to the shock-reflection pattern, and the effects of the combined thermal and viscous boundary layer on the reflection process will be dominant. As the shock-refection pattern grows, the Reynolds number will increase, and the boundary-layer thickness will become a smaller part of the shock-reflection pattern, and the boundary-layer effects on the shock-reflection process will thereby diminish. As the Reynolds number increases toward infinity as the shock-reflection pattern grows unboundedly, the boundary-layer effects on the reflected shock-reflection process will also diminish unboundedly and become insignificant.

Note that for the case of a turbulent boundary layer the viscous length ratio and Reynolds number would decay more slowly as $(\ell_v/z)^{1/5}$ and $\text{Re}_z^{-1/5}$, respectively. Hence, the effects of the turbulent boundary layer on the reflected shock process would diminish more slowly with time and take somewhat longer to become insignificant. These conclusions for the RR wave pattern should also carry over to the other more complicated wave patterns of SMR, TMR, and DMR.

The implications of these boundary-layer effects on shock reflections from wedges alter previous thinking of the transition boundary between regular to Mach reflections for both viscous and inviscid flows. Consider the case of an incident shock, with a Mach number $M_i = 2.327$, reflecting from an inclined ramp of angle $\theta_w = 52°$, which was a test case for numerical and experimental studies of Henderson et al. [11]. The incident shock encounters the wedge apex, diffracts, and starts to move along the wedge. The thermal and viscous effects of the shock-induced boundary layer are initially very large, because $\text{Re}_z \approx 0$. The reflected shock pattern is forced to start as a regular reflection, because of the strong boundary-layer effects, which results in a spatial separation between the corner wave and the co-joined incident and reflected shocks at the wedge surface. As the incident shock moves forward, the shock-reflection flow field expands with time, and the shock-induced boundary-layer effects on the shock-

reflection process subside somewhat, because Re_z increases. The corner wave is not held back or retarded as much, so the spatial separation between the corner wave and co-joined leading shocks decreases. Eventually, as the reflected shock system expands further with time, the boundary-layer effects diminish further, because Re_z increases further so that the corner signal finally overtakes the co-joined incident and reflected shocks, and a Mach-reflection pattern then emerges and expands with time. As the Mach reflection pattern continues to grow, the boundary-layer effects continue to diminish, and they eventually become negligible as $Re_z \to \infty$.

The preceding explanation of a regular reflection transitioning into a Mach reflection at some distance along the wedge surface is consistent with the experimental and numerical experiments reported in Henderson et al. [24] and Henderson et al. [11] for argon, and Kobayashi et al. [12] for air. For the case of argon, the process gives one transition-boundary point labeled $\theta^v = 52°$ in Fig. 18 for a wedge that is 0.17 m long, and for air the corresponding transition points are included in Fig. 3. Note that the explanation given here for the transition from RR to MR does not require a definition of precursor regular reflection (PRR) and a description of the corner wave as being unstable or metastable by Henderson et al. [11] to help explain their "unexpected" corner-wave motion on overtaking the leading shocks. Furthermore, the hidden assumption in the previous study is removed that the effects of the boundary layer on the shock-reflection flow field are constant with time and independent of the size of the shock-reflection pattern.

Now, consider the case of the same-strength incident shock ($M_i = 2.327$) reflecting from a wedge in which the wedge angle is increased from $52°$ to $53°$. One might surmise that the starting regular-reflection pattern might persist all along the wedge to its very end at 0.17 m, because the boundary-layer effects dominate and the corner wave cannot overtake the leading shocks and form a Mach reflection pattern before the end of the 0.17-m-long wedge is encountered. However, if the wedge length is increased, then the effects of the boundary layer on the shock-reflection flow field will diminish further with time, and a Mach reflection will then emerge for this longer wedge. This thought process implies that the transition boundary between RR and MR has shifted to $53°$ for this longer wedge. One can continue this thought process of increasing the wedge angle, for a constant incident shock Mach number, and conclude that the RR-to-MR transition boundary shifts once again to the larger wedge angle for a longer wedge. However, once the process of increasing the wedge angle approaches the present authors' numerical transition boundary, denoted by θ_n^i in Fig. 18, the wedge lengths should approach infinity for the shock-induced boundary-layer effects to become negligible, such that a Mach-reflection pattern could eventually emerge at the end of an infinitely long ramp. This is pre-

cisely when the transition boundary for inviscid flow without a boundary layer is approached, which corresponds to the case when $Re_z \to \infty$.

This discussion above leads to some important conclusions. Firstly, the transition boundary that separates regular and Mach reflections for a moving incident shock of constant strength and interacting with a wedge with a boundary layer (from a smooth or rough surface) will be affected by the wedge length. In other words, the RR-to-MR transition boundary is wedge length and surface roughness dependent. For the case of the shock-tube reflection experiments from wedges in air, the fairly closely banded experimental data shown in Fig. 3 are typically for wedge lengths ranging from 0.05 to 0.15 m and for wedges that are relatively smooth (polished). For the effects of moderate to strong wedge-surface roughnesses that result in a widely spaced experimental data in plots of wedge angle versus shock strength, see Ben-Dor [4] and Reichenbach [41]. One should be able to produce additional experimental data for additional RR-to-MR reflection boundaries between the currently available experimental data and the new numerical boundary by simultaneously slightly increasing the wedge angle and lengthening the wedge for a set of fixed incident shock Mach numbers.

Secondly, the upward limit of the transition boundary between RR and MR for viscous flows in gases (diatomic, monatomic, and others) should become that for an infinite wedge length at the present authors' transition boundary (or some other not yet determined numerical transition boundary). As a consequence, the authors have intentionally focused their attention and efforts to date on determining accurately the transition boundary between RR and MR for wedges without a boundary layer in diatomic and monatomic gases (i.e., the limiting self-similar viscous solutions for very long times for a long wedge with $Re_z \to \infty$), because of the importance of this limiting transition boundary for both inviscid and viscous flows.

Although the significance of the computed inviscid transition boundary between RR and MR was established herein using a variation in well-known and elegant scaling principles for the boundary-layer influence on the shock-reflection pattern and resulting transition boundary, the results of this analysis were recognized previously in a somewhat different but parallel context. The effects of both real gases and the combined viscous and thermal boundary layer were well known to shift the transition boundary between RR and MR downwards below the extreme-angle boundary of von Neumann. For example, see the work for straight wedges by Hornung and Taylor [39] on the effects of the boundary layer; Lee and Glass [42], Shirouzu and Glass [43], and Glass' student Wheeler [44] on equilibrium-air and boundary-layer effects; and also Ben-Dor [4] who includes his and other researchers work of this type in his books.

For the case of a shock interacting with a cylinder, see the book by Ben-Dor[4] for a collection and discussion of relevant data; and the paper by Kleine et al.[45] for the effects of the boundary layer and pre-shock-reflection pressure on the Mach-stem trajectory and height. Kleine et al.[45] were able to clearly show and conclude that the viscous effects on the Mach-stem height diminished as the cylinder diameter and pre-shock pressure increased their Reynolds number, such that the Mach-stem trajectories converged to the Mach-stem trajectory for the case of inviscid flow. These numerical and experimental studies have identified the shift of the transition boundary and Mach-stem trajectory and height by changes in the Reynolds number, which is somewhat parallel and equivalent to the present authors' more comprehensive description of multiple transition boundaries for the case of viscous flows, meaning that the transition boundary for viscous flows is wedge length and wedge-surface roughness dependent.

References

1. von Neumann, J.: Oblique reflection of shocks. Explosive Research Report No. 12, Navy Department, Bureau of Ordnance, U.S. Department of Communication Technology Services No. PB37079 (1943) (John von Neumann, Collected Works). Pergamon Press, Oxford, vol. 6, pp. 238–299 (1963)

2. Ben-Dor, G., Glass, I.I.: Domains and boundaries of nonstationary oblique shock-wave reflexions. 1. Diatomic gas. J. Fluid Mech. **92**(3), 459–496 (1979). https://doi.org/10.1017/S0022112079000732

3. Ben-Dor, G., Glass, I.I.: Domains and boundaries of nonstationary oblique shock-wave reflexions. 2. Monatomic gas. J. Fluid Mech. **96**(4), 735–756 (1980). https://doi.org/10.1017/S0022112080002339

4. Ben-Dor, G.: Shock Wave Reflection Phenomena, 1e, 2e. Springer, Berlin (1991, 2007). ISBN 978-3-540-71381-4. https://doi.org/10.1007/978-1-4757-4279-4

5. Glass, I.I., Sislian, J.P.: Nonstationary Flows and Shock Waves. Clarendon Press, Oxford (1994)

6. Colella, P., Henderson, L.F.: The von Neumann paradox for the diffraction of weak shock waves. J. Fluid Mech. **213**, 71–94 (1990). https://doi.org/10.1017/S0022112090002221

7. Semenov, A.N., Berezkina, M.K., Krassovskaya, I.V.: Classification of pseudo-steady shock wave reflection types. Shock Waves **22**(4), 307–316 (2012). https://doi.org/10.1007/s00193-012-0373-z

8. Hornung, H.: Regular and Mach reflection of shock waves. Annu. Rev. Fluid Mech. **18**, 33–58 (1986). https://doi.org/10.1146/annurev.fl.18.010186.000341

9. Bleakney, W., Taub, A.H.: Interaction of shock waves. Rev. Mod. Phys. **21**(4), 584–605 (1949). https://doi.org/10.1103/RevModPhys.21.584

10. Kawamura, R., Saito, H.: Reflection of shock waves—1. Pseudo-stationary case. J. Phys. Soc. Jpn. **11**(5), 584–592 (1956). https://doi.org/10.1143/JPSJ.11.584

11. Henderson, L.F., Takayama, K., Crutchfield, W.Y., Itabashi, S.: The persistence of regular reflection during strong shock diffraction over rigid ramps. J. Fluid Mech. **431**, 273–296 (2001). https://doi.org/10.1017/S0022112000003165

12. Kobayashi, S., Adachi, T., Suzuki, T.: On the unsteady transition phenomenon of weak shock waves. Theor. Appl. Mech. Jpn. **49**, 271–278 (2000)

13. Smith, L.G.: Photographic investigation of the reflection of plane shocks in air. Division 2, National Defence Research Committee of the Office of Scientific Research and Development, OSRD Report No. 6271 (1945)

14. Henderson, L.F., Lozzi, A.: Experiments on transition of Mach reflexion. J. Fluid Mech. **68**(1), 139–155 (1975). https://doi.org/10.1017/S0022112075000730

15. Henderson, L.F., Siegenthaler, A.: Experiments on the diffraction of weak blast waves: the von Neumann paradox. Proc. R. Soc. Lond. A **369**(1739), 537–555 (1980). https://doi.org/10.1098/rspa.1980.0015

16. Walker, D.K., Dewey, J.M., Scotten, L.N.: Observation of density discontinuities behind reflected shocks close to the transition from regular to Mach reflection. J. Appl. Phys. **53**(3), 1398–1400 (1982). https://doi.org/10.1063/1.329871

17. Lock, G.D., Dewey, J.M.: An experimental investigation of the sonic criterion for transition from regular to Mach reflection of weak shock waves. Exp. Fluids **7**(5), 289–292 (1989). https://doi.org/10.1007/BF00198446

18. Smith, W.R.: Mutual reflection of two shock waves of arbitrary strengths. Phys. Fluids **2**(5), 533–541 (1959). https://doi.org/10.1063/1.1705945

19. Henderson, L.F., Lozzi, A.: Further experiments on transition to Mach reflexion. J. Fluid Mech. **94**(3), 541–559 (1979). https://doi.org/10.1017/S0022112079001178

20. Barbosa, F.J., Skews, B.W.: Experimental confirmation of the von Neumann theory of shock wave reflection transition. J. Fluid Mech. **472**, 263–282 (2002). https://doi.org/10.1017/S0022112002002343

21. Herron, T., Skews, B.: On the persistence of regular reflection. Shock Waves **21**(6), 573–578 (2011). https://doi.org/10.1007/s00193-011-0341-z

22. Hryniewicki, M.K., Gottlieb, J.J., Groth, C.P.T.: Transition boundary between regular and Mach reflections for a moving shock interacting with a wedge in inviscid and polytropic air. Shock Waves **27**(4), 523–550 (2017). https://doi.org/10.1007/s00193-016-0697-1

23. Alzamora Previtali, F., Timofeev, E., Kleine, H.: On unsteady shock wave reflections from wedges with straight and concave tips. 45th AIAA Fluid Dynamics Conference, Dallas, TX, AIAA Paper 2015-2642 (2015). https://doi.org/10.2514/6.2015-2642

24. Henderson, L.F., Crutchfield, W.Y., Virgona, R.J.: The effects of thermal conductivity and viscosity of argon on shock waves diffracting over rigid ramps. J. Fluid Mech. **331**, 1–36 (1997). https://doi.org/10.1017/S0022112096003850

25. Thompson, P.A.: Compressible-Fluid Dynamics. Rensselaer Polytechnic Institute Press, New York (1988)

26. Courant, R., Friedrichs, K.O.: Supersonic Flow and Shock Waves. Interscience Publisher, New York (1948)

27. Hryniewicki, M.K., Groth, C.P.T., Gottlieb, J.J.: Parallel implicit anisotropic block-based adaptive mesh refinement finite-volume scheme for the study of fully resolved oblique shock wave reflections. Shock Waves **25**(4), 371–386 (2015). https://doi.org/10.1007/s00193-015-0572-5

28. Freret L., Groth, C.P.T.: Anisotropic non-uniform block-based adaptive mesh refinement for three-dimensional inviscid and viscous flows. 22nd AIAA Computational Fluid Dynamics Conference, Dallas, TX, AIAA Paper 2015-2613 (2015). https://doi.org/10.2514/6.2015-2613

29. McDonald, J.G., Sachdev, J.S., Groth, C.P.T.: Application of Gaussian moment closure to microscale flows with moving embedded boundaries. AIAA J. **52**(9), 1839–1857 (2014). https://doi.org/10.2514/1.J052576

30. Northrup, S.A., Groth, C.P.T.: Parallel implicit adaptive mesh refinement scheme for unsteady fully-compressible reactive flows. 21st AIAA Computational Fluid Dynamics Conference, Fluid Dynamics and Co-located Conferences, San Diego, CA, AIAA Paper 2013-2433 (2013). https://doi.org/10.2514/6.2013-2433

31. Williamschen, M.J., Groth, C.P.T.: Parallel anisotropic block-based adaptive mesh refinement algorithm for three-dimensional flows. 21st AIAA Computational Fluid Dynamics Conference, Fluid Dynamics and Co-located Conferences, San Diego, CA, AIAA Paper 2013-2442 (2013). https://doi.org/10.2514/6.2013-2442

32. Zhang, Z.J., Groth, C.P.T.: Parallel high-order anisotropic block-based adaptive mesh refinement finite-volume scheme. 20th AIAA Computational Fluid Dynamics Conference, Fluid Dynamics and Co-located Conferences, Honolulu, HI, AIAA Paper 2011-3695 (2011). https://doi.org/10.2514/6.2011-3695

33. Gao, X., Northrup, S.A., Groth, C.P.T.: Parallel solution-adaptive method for two-dimensional non-premixed combusting flows. Prog. Comput. Fluid Dyn. **11**(2), 76–95 (2011). https://doi.org/10.1504/PCFD.2011.038834

34. Gao, X., Groth, C.P.T.: A parallel solution-adaptive scheme for three-dimensional turbulent non-premixed combusting flows. J. Comput. Phys. **229**(9), 3250–3275 (2010). https://doi.org/10.1016/j.jcp.2010.01.001

35. Gao, X., Groth, C.P.T.: A parallel adaptive mesh refinement algorithm for predicting turbulent non-premixed combusting flows. Int. J. Comput. Fluid Dyn. **20**(5), 349–357 (2006). https://doi.org/10.1080/10618560600917583

36. Sachdev, J.S., Groth, C.P.T., Gottlieb, J.J.: A parallel solution-adaptive scheme for multi-phase core flows in solid propellant rocket motors. Int. J. Comput. Fluid Dyn. **19**(2), 159–177 (2005). https://doi.org/10.1080/10618560410001729135

37. Hryniewicki, M.K.: On the transition boundary between regular and Mach reflections from a wedge in inviscid and polytropic gases. PhD Thesis, UTIAS, University of Toronto (2016)

38. von Becker, E.: Instationäre grenzschichten hinter verdichtungsstößen und expansionswellen. Prog. Aerosp. Sci. **1**, 104–173 (1961). https://doi.org/10.1016/0376-0421(61)90005-7

39. Hornung, H.G., Taylor, J.R.: Transition from regular to Mach reflection of shock waves. Part 1. The effect of viscosity in the pseudosteady case. J. Fluid Mech. **123**, 143–153 (1982). https://doi.org/10.1017/S0022112082002997

40. Hornung, H.: The effect of viscosity on the Mach stem length in unsteady strong shock reflection. In: Meier, G.E.A., Obermeier, F. (eds.) Flow of Real Fluids. Lecture Notes in Physics, vol. 235, pp. 82–91. Springer, Berlin (1985). https://doi.org/10.1007/3-540-15989-4_73

41. Reichenbach, H.: Roughness and heated-layer effects on shock-wave propagation and reflection—experimental results. Ernst Mach Institute, EMI Report E24/85. West Germany, Freiburg (1985)

42. Lee, J.-H., Glass, I.I.: Pseudo-stationary oblique-shock-wave reflections in frozen and equilibrium air. Prog. Aerosp. Sci. **21**(1), 33–80 (1984). https://doi.org/10.1016/0376-0421(84)90003-4

43. Shirouzu, M., Glass, I.I.: Evaluation of assumptions and criteria in pseudostationary oblique shock-wave reflections. Proc. R. Soc. Lond. A **406**(1830), 75–92 (1986). https://doi.org/10.1098/rspa.1986.0065

44. Wheeler, J.: An interferometric investigation of the regular to Mach reflection transition boundary in pseudostationary flow in air. UTIAS Technical Note No. 256, University of Toronto Institute for Aerospace Studies (1986)

45. Kleine, H., Timofeev, E., Hakkaki-Fard, A., Skews, B.: The influence of Reynolds number on the triple point trajectories at shock reflection off cylindrical surfaces. J. Fluid Mech. **740**, 47–60 (2014). https://doi.org/10.1017/jfm.2013.634